ACOUSTIC WAVE PROPAGATION IN AND AROUND A FLUID-FILLED BOREHOLE OF IRREGULAR CROSS-SECTION

by

Chengbin Peng[1] and C.H. Cheng

Earth Resources Laboratory
Department of Earth, Atmospheric, and Planetary Sciences
Massachusetts Institute of Technology
Cambridge, MA 02139

ABSTRACT

Boreholes with 10% or more ellipticity are not uncommon. In this paper, we consider the coupling of an incident elastic wave into a borehole of irregular cross-section and investigate the cross-mode coupling phenomenon in sonic well logging in the presence of borehole irregularity. The mode-matching method is used. Different from its original formulation, we employ the Reichel et al. algorithm to obtain the discrete least square approximation by trigonometric polynomials, a technique closely related to the fast Fourier transform (FFT). Our method not only yields great accuracy but also gains computational speed. Our study shows that the pressure in the borehole fluid is sensitive to the irregularity of the borehole cross-section, it is larger if the incident wave is along the effective minor axis and smaller if the incident wave is along the effective major axis. In the frequency range of a typical borehole experiment, the solid displacement in the formation is much less affected by the borehole irregularity. In an elliptical borehole, a monopole source excites dipole wave trains that are characteristic of the tube waves, and a centered dipole source excites monopole wave trains that are characteristic of the flexural waves.

INTRODUCTION

It has been observed that the boreholes drilled into the earth are noncircular and often of irregular shape (Hilchie et al., 1968; Dart et al., 1989; among others). Elastic wave propagation in a noncircular borehole attracted some attention in recent years. For the low frequency limit, Zimmerman (1986) and Norris (1990) proposed a method to calculate the tube wave velocity in a borehole of arbitrary cross-section. They found that the tube wave speed is reduced compared to the one in a circular borehole. Ellefsen (1990) applied a perturbation method to study higher order mode dispersion in an elliptical borehole. He noticed that the percent change in phase velocity at any frequency was small in a slightly irregular borehole. Randall (1991a) calculated the dispersion

[1]Presently at the Geophysics Research Department, Bellaire Research Center, Shell Development Company, P. O. Box 481, Houston TX 77001-0481.

curves for modes in a noncircular fluid-filled borehole in elastic formations by using the boundary integral formulation. He found that the flexural and screw modes split into two distinct branches delineated by their orientations. Using the same method, Randall (1991b) and Liu and Randall (1991) computed the dipole sonic logs in an elliptical borehole.

The goal of this paper is to study the coupling between an incident elastic wave and a fluid-filled borehole of irregular cross-section, in order to understand the effects of the borehole irregularity on downhole seismic measurements. We will apply a mode-matching method. Deviating from the original formulation (Okuno, 1990), we will employ an algorithm by Reichel et al. (1991) (hereinafter referred to as the Reichel et al. algorithm in the text). This algorithm solves a discrete least squares approximation by trigonometric polynomials, a technique closely related to the fast Fourier transform. Compared to the boundary integral formulation (Randall, 1991a, 1991b), our method is faster because the number of unknowns to be determined is decreased by an order of magnitude. The method proposed in this paper will also be applied to compute synthetic sonic logs in a borehole of an irregular cross-section. In the latter application, multiple sources and arrays of multipole receivers will be used. The synthetic logging seismograms will be computed to study the cross-mode coupling phenomenon in the presence of irregular cross-section of the borehole, which may be mistakenly attributed to formation anisotropy (Hatchell and Cowles, 1992).

This paper includes four sections. In the first section, we will give a theoretical formulation for elastic wave scattering in a fluid-filled borehole, using the mode-matching method as well as the Reichel et al. algorithm. We will also address issues concerning its implementation on a computer. In the next two sections, we will present some numerical examples of elastic wave coupling and synthetic sonic logging seismograms in a noncircular borehole, respectively. In the last section, we will give a brief discussion and draw some conclusions.

THEORETICAL FORMULATIONS FOR ELASTIC WAVE PROPAGATION IN IRREGULAR BOREHOLES

Consider an elastic plane wave incident upon an infinite fluid-filled borehole, as shown in Figure 1. The cross-section of the borehole is irregular. The formation is homogeneous and elastic with compressional wave speed α, shear wave speed β, and density ρ. The borehole is filled with a fluid of density ρ_f and compressional wave speed α_f. The radius of the borehole is parameterized by the following trigonometric series:

$$r(\theta) = r_0 + \sum_{l=1}^{L} (r_a(l) \cos l\theta + r_b(l) \sin l\theta). \tag{1}$$

The objective is to compute the pressure in the fluid and the solid displacements on the borehole wall for a source in the formation. And conversely, as applications to sonic well logging, we also compute the full acoustic waveforms for a multiple source in the borehole.

Modal Solutions

The general solutions to the displacement potentials in both fluid (ϕ_f) and solid (ϕ, ξ and ψ) can be expressed in a cylindrical coordinate system as (Schoenberg, 1986) [2]

$$\phi_f = -\frac{\alpha_f V(\omega)}{\omega^2}\,[\,A_0\;J_0(k_f r) + 2\sum_{n=1}^{\infty} i^n (A_n\,\cos n\theta + A_n^{'}\,\sin n\theta)\;J_n(k_f r)\,], \tag{2a}$$

$$\phi = -\frac{\alpha V(\omega)}{\omega^2}\,[\,B_0\;H_0^{(1)}(k_p r) + 2\sum_{n=1}^{\infty} i^n (B_n\,\cos n\theta + B_n^{'}\,\sin n\theta)\;H_n^{(1)}(k_p r)\,], \tag{2b}$$

$$\xi = -\frac{i\beta^2 V(\omega)}{\omega^3}\,[\,C_0\;H_0^{(1)}(k_s r) + 2\sum_{n=1}^{\infty} i^n (C_n\,\cos n\theta + C_n^{'}\,\sin n\theta)\;H_n^{(1)}(k_s r)\,], \tag{2c}$$

$$\psi = -\frac{\beta V(\omega)}{\omega^2}\,[\,-D_0^{'}\;H_0^{(1)}(k_s r) + 2\sum_{n=1}^{\infty} i^n (D_n\,\sin n\theta - D_n^{'}\,\cos n\theta)\;H_n^{(1)}(k_s r)\,], \tag{2d}$$

where z dependence and time dependence $e^{i(k_z z - \omega t)}$ is assumed. In these equations, $k_f = \sqrt{\omega^2/\alpha_f^2 - {k_z}^2}$, $k_p = \sqrt{\omega^2/\alpha^2 - {k_z}^2}$ and $k_s = \sqrt{\omega^2/\beta^2 - {k_z}^2}$ are the radial wavenumbers in the fluid and solid, respectively. The signs of k_f, k_p, k_z are chosen such that the imaginary part $\mathbf{Im}(k_p,\, k_s,\, k_f) \geq 0$. $V(\omega)$ ($\equiv -\omega^2$, without loss of generality) denotes the source function at a given frequency ω.

For this problem, the boundary conditions are the continuities of normal displacement $u_n(r^{\pm}, \theta)$ and normal stress $\sigma_{nn}(r^{\pm}, \theta)$, and vanishing of tangential stresses $\sigma_{nb}(r^{\pm}, \theta)$ and $\sigma_{nz}(r^{\pm}, \theta)$ at the borehole wall $r = r^{\pm}(\theta)$, that is,

$$u_n^{(f)}(r^-, \theta) = u_n^{(s)}(r^+, \theta) + u_n^{(i)}(r^+, \theta), \tag{3a}$$

$$-\,p^{(f)}(r^-, \theta) = \sigma_{nn}^{(s)}(r^+, \theta) + \sigma_{nn}^{(i)}(r^+, \theta), \tag{3b}$$

$$\sigma_{nb}^{(s)}(r^+, \theta) + \sigma_{nb}^{(i)}(r^+, \theta) = 0, \tag{3c}$$

$$\sigma_{nz}^{(s)}(r^+, \theta) + \sigma_{nz}^{(i)}(r^+, \theta) = 0. \tag{3d}$$

In the above expressions, the superscript (i) denotes the quantities associated with the incident wave, (s) denotes those of the scattered wave in the solid and (f) those in the fluid. The pressure in the fluid is denoted by p. A local coordinate frame is used where $\mathbf{n}$ is normal to the borehole boundary, $\mathbf{b}$ is tangential to the boundary, and $\mathbf{z}$ is in the axial direction (see Figure 1).

The transformation from the cylindrical coordinates $(\mathbf{r}, \theta, \mathbf{z})$ to the local orthogonal coordinates $(\mathbf{n}, \mathbf{b}, \mathbf{z})$ on the boundary is accomplished through an angular rotation $\varphi = <\mathbf{n}, \mathbf{r}>$, which is given by

$$\varphi = \tan^{-1}\,\frac{\sum_{l=1}^{L} l\,(\,-r_a(l)\sin l\theta + r_b(l)\cos l\theta\,)}{r_0 + \sum_{l=1}^{L}(\,r_a(l)\cos l\theta + r_b(l)\sin l\theta\,)}. \tag{4}$$

[2] No energy from ∞ is included in the solution. This may not be true if the borehole cross-section is highly irregular such that multiply scattered energies travel inward.

We transform the displacements and stresses from the cylindrical coordinates $(\mathbf{r}, \theta, \mathbf{z})$ to the local orthogonal coordinates $(\mathbf{n}, \mathbf{b}, \mathbf{z})$ using the following relations:

$$\begin{bmatrix} u_n \\ u_b \\ u_z \end{bmatrix} = \begin{bmatrix} \cos\varphi & \sin\varphi & 0 \\ -\sin\varphi & \cos\varphi & 0 \\ 0 & 0 & 1 \end{bmatrix} \begin{bmatrix} u_r \\ u_\theta \\ u_z \end{bmatrix},$$

and

$$\begin{bmatrix} \sigma_{nn} & \sigma_{nb} & \sigma_{nz} \\ \sigma_{bn} & \sigma_{bb} & \sigma_{bz} \\ \sigma_{zn} & \sigma_{zb} & \sigma_{zz} \end{bmatrix} = \begin{bmatrix} \cos\varphi & \sin\varphi & 0 \\ -\sin\varphi & \cos\varphi & 0 \\ 0 & 0 & 1 \end{bmatrix} \begin{bmatrix} \sigma_{rr} & \sigma_{r\theta} & \sigma_{rz} \\ \sigma_{\theta r} & \sigma_{\theta\theta} & \sigma_{\theta z} \\ \sigma_{zr} & \sigma_{z\theta} & \sigma_{zz} \end{bmatrix} \begin{bmatrix} \cos\varphi & -\sin\varphi & 0 \\ \sin\varphi & \cos\varphi & 0 \\ 0 & 0 & 1 \end{bmatrix}.$$

Upon these rotations, expressions for the normal displacement and tractions on the boundary are obtained. In terms of harmonic expansions, they are given by:

$$\begin{aligned} u_n^{(f)}(r,\theta) &= \sum_{n=0}^{\infty} i^n \varepsilon_n \mathcal{U}_n^{(f)}(r) \left[A_n \cos n\theta + A_n' \sin n\theta \right] \cos\phi \\ &+ \sum_{n=0}^{\infty} i^n \varepsilon_n \mathcal{V}_n^{(f)}(r) \left[-A_n \sin n\theta + A_n' \cos n\theta \right] \sin\phi, \end{aligned} \tag{5a}$$

$$\begin{aligned} u_n^{(s)}(r,\theta) &= \sum_{n=0}^{\infty} i^n \varepsilon_n \mathcal{U}_n^{(\phi)}(r) \left[B_n \cos n\theta + B_n' \sin n\theta \right] \cos\phi \\ &+ \sum_{n=0}^{\infty} i^n \varepsilon_n \mathcal{V}_n^{(\phi)}(r) \left[-B_n \sin n\theta + B_n' \cos n\theta \right] \sin\phi \\ &+ \sum_{n=0}^{\infty} i^n \varepsilon_n \mathcal{U}_n^{(\xi)}(r) \left[C_n \cos n\theta + C_n' \sin n\theta \right] \cos\phi \\ &+ \sum_{n=0}^{\infty} i^n \varepsilon_n \mathcal{V}_n^{(\xi)}(r) \left[-C_n \sin n\theta + C_n' \cos n\theta \right] \sin\phi \\ &+ \sum_{n=0}^{\infty} i^n \varepsilon_n \mathcal{U}_n^{(\psi)}(r) \left[D_n \cos n\theta + D_n' \sin n\theta \right] \cos\phi \\ &+ \sum_{n=0}^{\infty} i^n \varepsilon_n \mathcal{V}_n^{(\psi)}(r) \left[-D_n \sin n\theta + D_n' \cos n\theta \right] \sin\phi, \end{aligned} \tag{5b}$$

$$-p^{(f)}(r,\theta) = \sigma_{nn}^{(f)}(r,\theta) = \sum_{n=0}^{\infty} i^n \varepsilon_n \mathcal{R}_n^{(f)}(r) \left[A_n \cos n\theta + A_n' \sin n\theta \right], \tag{5c}$$

$$\begin{aligned} \sigma_{nn}^{(s)}(r,\theta) &= \sum_{n=0}^{\infty} i^n \varepsilon_n \mathcal{R}_n^{(\phi)}(r) \left[B_n \cos n\theta + B_n' \sin n\theta \right] \cos^2\phi \\ &+ \sum_{n=0}^{\infty} i^n \varepsilon_n \mathcal{T}_n^{(\phi)}(r) \left[-B_n \sin n\theta + B_n' \cos n\theta \right] \sin 2\phi \\ &+ \sum_{n=0}^{\infty} i^n \varepsilon_n \mathcal{M}_n^{(\phi)}(r) \left[B_n \cos n\theta + B_n' \sin n\theta \right] \sin^2\phi \end{aligned}$$

$$
\begin{aligned}
&+ \sum_{n=0}^{\infty} i^n \, \varepsilon_n \, \mathcal{R}_n^{(\xi)}(r) \, [\, C_n \, \cos n\theta + C'_n \, \sin n\theta \,] \, \cos^2\phi \\
&+ \sum_{n=0}^{\infty} i^n \, \varepsilon_n \, \mathcal{T}_n^{(\xi)}(r) \, [\, -C_n \, \sin n\theta + C'_n \, \cos n\theta \,] \, \sin 2\phi \\
&+ \sum_{n=0}^{\infty} i^n \, \varepsilon_n \, \mathcal{M}_n^{(\xi)}(r) \, [\, C_n \, \cos n\theta + C'_n \, \sin n\theta \,] \, \sin^2\phi \\
&+ \sum_{n=0}^{\infty} i^n \, \varepsilon_n \, \mathcal{R}_n^{(\psi)}(r) \, [\, D_n \, \cos n\theta + D'_n \, \sin n\theta \,] \, \cos^2\phi \\
&+ \sum_{n=0}^{\infty} i^n \, \varepsilon_n \, \mathcal{T}_n^{(\psi)}(r) \, [\, -D_n \, \sin n\theta + D'_n \, \cos n\theta \,] \, \sin 2\phi \\
&+ \sum_{n=0}^{\infty} i^n \, \varepsilon_n \, \mathcal{M}_n^{(\psi)}(r) \, [\, D_n \, \cos n\theta + D'_n \, \sin n\theta \,] \, \sin^2\phi, \qquad \text{(5d)}
\end{aligned}
$$

$$
\begin{aligned}
\sigma_{nb}^{(s)}(r,\theta) \;=\; & \sum_{n=0}^{\infty} i^n \, \varepsilon_n \, \frac{[\, \mathcal{M}_n^{(\phi)}(r) - \mathcal{R}_n^{(\phi)}(r) \,]}{2} \, [\, B_n \, \cos n\theta + B'_n \, \sin n\theta \,] \, \sin 2\phi \\
&+ \sum_{n=0}^{\infty} i^n \, \varepsilon_n \, \mathcal{T}_n^{(\phi)}(r) \, [\, -B_n \, \sin n\theta + B'_n \, \cos n\theta \,] \, \cos 2\phi \\
&+ \sum_{n=0}^{\infty} i^n \, \varepsilon_n \, \frac{[\, \mathcal{M}_n^{(\xi)}(r) - \mathcal{R}_n^{(\xi)}(r) \,]}{2} \, [\, C_n \, \cos n\theta + C'_n \, \sin n\theta \,] \, \sin 2\phi \\
&+ \sum_{n=0}^{\infty} i^n \, \varepsilon_n \, \mathcal{T}_n^{(\xi)}(r) \, [\, -C_n \, \sin n\theta + C'_n \, \cos n\theta \,] \, \cos 2\phi \\
&+ \sum_{n=0}^{\infty} i^n \, \varepsilon_n \, \frac{[\, \mathcal{M}_n^{(\psi)}(r) - \mathcal{R}_n^{(\psi)}(r) \,]}{2} \, [\, D_n \, \cos n\theta + D'_n \, \sin n\theta \,] \, \sin 2\phi \\
&+ \sum_{n=0}^{\infty} i^n \, \varepsilon_n \, \mathcal{T}_n^{(\psi)}(r) \, [\, -D_n \, \sin n\theta + D'_n \, \cos n\theta \,] \, \cos 2\phi, \qquad \text{(5e)}
\end{aligned}
$$

$$
\begin{aligned}
\sigma_{nz}^{(s)}(r,\theta) \;=\; & \sum_{n=0}^{\infty} i^n \, \varepsilon_n \, \mathcal{Z}_n^{(\phi)}(r) \, [\, B_n \, \cos n\theta + B'_n \, \sin n\theta \,] \, \cos\phi \\
&+ \sum_{n=0}^{\infty} i^n \, \varepsilon_n \, \mathcal{N}_n^{(\phi)}(r) \, [\, -B_n \, \sin n\theta + B'_n \, \cos n\theta \,] \, \sin\phi \\
&+ \sum_{n=0}^{\infty} i^n \, \varepsilon_n \, \mathcal{Z}_n^{(\xi)}(r) \, [\, C_n \, \cos n\theta + C'_n \, \sin n\theta \,] \, \cos\phi \\
&+ \sum_{n=0}^{\infty} i^n \, \varepsilon_n \, \mathcal{N}_n^{(\xi)}(r) \, [\, -C_n \, \sin n\theta + C'_n \, \cos n\theta \,] \, \sin\phi \\
&+ \sum_{n=0}^{\infty} i^n \, \varepsilon_n \, \mathcal{Z}_n^{(\psi)}(r) \, [\, D_n \, \cos n\theta + D'_n \, \sin n\theta \,] \, \cos\phi \\
&+ \sum_{n=0}^{\infty} i^n \, \varepsilon_n \, \mathcal{N}_n^{(\psi)}(r) \, [\, -D_n \, \sin n\theta + D'_n \, \cos n\theta \,] \, \sin\phi, \qquad \text{(5f)}
\end{aligned}
$$

where $\epsilon_n = \begin{cases} 1 & \text{if } n = 0 \\ 2 & \text{if } n \geq 1 \end{cases}$ is the Newmann factor. The radial dependences $\mathcal{U}_n^{(f)}(r), \mathcal{U}_n^{(\phi)}(r)$, ..., $\mathcal{Z}_n^{(\psi)}(r), \mathcal{N}_n^{(\psi)}(r)$ have been given in Appendix A.

Unlike the case of a circular borehole where the boundary conditions are satisfied by each individual mode in the harmonic expansions (2a)-(2d), in a noncircular borehole it is the total field that satisfies the boundary conditions. A least square formalism is used to determine the unknown coefficients $\{A_n, A_n', B_n, B_n', C_n, C_n', D_n, D_n'\}$ such that the errors in satisfying the boundary conditions are as small as possible.

Fourier Series Expansion

We expand the normal displacements and the normal as well as tangential stresses on the boundary $r^+ = r^- = r(\theta)$ in terms of Fourier series. The results for the normal displacements are:

$$u_n^{(f)}(r^-, \theta) = a_0 + \sum_{l=1}^{\infty} (a_l \cos l\theta + a_l' \sin l\theta), \tag{6a}$$

$$\begin{aligned} u_n^{(s)}(r^+, \theta) &= b_0 + \sum_{l=1}^{\infty} (b_l \cos l\theta + b_l' \sin l\theta) \\ &+ c_0 + \sum_{l=1}^{\infty} (c_l \cos l\theta + c_l' \sin l\theta) \\ &+ d_0 + \sum_{l=1}^{\infty} (d_l \cos l\theta + d_l' \sin l\theta), \end{aligned} \tag{6b}$$

where

$$a_l = \left(\underline{\underline{a_{11}}}\right)_{ln} A_n + \left(\underline{\underline{a_{12}}}\right)_{ln} A_n'; \qquad a_l' = \left(\underline{\underline{a_{21}}}\right)_{ln} A_n + \left(\underline{\underline{a_{22}}}\right)_{ln} A_n';$$

$$b_l = \left(\underline{\underline{b_{11}}}\right)_{ln} B_n + \left(\underline{\underline{b_{12}}}\right)_{ln} B_n'; \qquad b_l' = \left(\underline{\underline{b_{21}}}\right)_{ln} B_n + \left(\underline{\underline{b_{22}}}\right)_{ln} B_n';$$

$$c_l = \left(\underline{\underline{c_{11}}}\right)_{ln} C_n + \left(\underline{\underline{c_{12}}}\right)_{ln} C_n'; \qquad c_l' = \left(\underline{\underline{c_{21}}}\right)_{ln} C_n + \left(\underline{\underline{c_{22}}}\right)_{ln} C_n';$$

$$d_l = \left(\underline{\underline{d_{11}}}\right)_{ln} D_n + \left(\underline{\underline{d_{12}}}\right)_{ln} D_n'; \qquad d_l' = \left(\underline{\underline{d_{21}}}\right)_{ln} D_n + \left(\underline{\underline{d_{22}}}\right)_{ln} D_n'.$$

The elements of matrices $\underline{\underline{a_{11}}}, \underline{\underline{a_{12}}}, \ldots, \underline{\underline{d_{22}}}$ are the integrals of the corresponding modal functions for the displacements along the borehole boundary.

Similarly, the pressure on the fluid side of the borehole wall and the normal as well as tangential stresses on the solid side of the borehole wall can be written as

$$-p^{(f)}(r^-, \theta) = \sigma_{nn}^{(f)}(r^-, \theta) = e_0 + \sum_{l=1}^{\infty} (e_l \cos l\theta + e_l' \sin l\theta), \tag{7a}$$

$$\begin{aligned}\sigma_{nn}^{(s)}(r^+,\theta) &= f_0+\sum_{l=1}^{\infty}\left(f_l\cos l\theta+f_l'\sin l\theta\right)\\ &+ g_0+\sum_{l=1}^{\infty}\left(g_l\cos l\theta+g_l'\sin l\theta\right)\\ &+ h_0+\sum_{l=1}^{\infty}\left(h_l\cos l\theta+h_l'\sin l\theta\right),\end{aligned}\tag{7b}$$

$$\begin{aligned}\sigma_{nb}^{(s)}(r^+,\theta) &= o_0+\sum_{l=1}^{\infty}\left(o_l\cos l\theta+o_l'\sin l\theta\right)\\ &+ p_0+\sum_{l=1}^{\infty}\left(p_l\cos l\theta+p_l'\sin l\theta\right)\\ &+ q_0+\sum_{l=1}^{\infty}\left(q_l\cos l\theta+q_l'\sin l\theta\right),\end{aligned}\tag{8a}$$

and

$$\begin{aligned}\sigma_{nz}^{(s)}(r^+,\theta) &= r_0+\sum_{l=1}^{\infty}\left(r_l\cos l\theta+r_l'\sin l\theta\right)\\ &+ s_0+\sum_{l=1}^{\infty}\left(s_l\cos l\theta+s_l'\sin l\theta\right)\\ &+ t_0+\sum_{l=1}^{\infty}\left(t_l\cos l\theta+t_l'\sin l\theta\right),\end{aligned}\tag{8b}$$

where

$$\begin{aligned}
e_l &= \left(\underline{\underline{e_{11}}}\right)_{ln} A_n+\left(\underline{\underline{e_{12}}}\right)_{ln} A_n'; & e_l' &= \left(\underline{\underline{e_{21}}}\right)_{ln} A_n+\left(\underline{\underline{e_{22}}}\right)_{ln} A_n';\\
f_l &= \left(\underline{\underline{f_{11}}}\right)_{ln} B_n+\left(\underline{\underline{f_{12}}}\right)_{ln} B_n'; & f_l' &= \left(\underline{\underline{f_{21}}}\right)_{ln} B_n+\left(\underline{\underline{f_{22}}}\right)_{ln} B_n';\\
g_l &= \left(\underline{\underline{g_{11}}}\right)_{ln} C_n+\left(\underline{\underline{g_{12}}}\right)_{ln} C_n'; & g_l' &= \left(\underline{\underline{g_{21}}}\right)_{ln} C_n+\left(\underline{\underline{g_{22}}}\right)_{ln} C_n';\\
h_l &= \left(\underline{\underline{h_{11}}}\right)_{ln} D_n+\left(\underline{\underline{h_{12}}}\right)_{ln} D_n'; & h_l' &= \left(\underline{\underline{h_{21}}}\right)_{ln} D_n+\left(\underline{\underline{h_{22}}}\right)_{ln} D_n';\\
o_l &= \left(\underline{\underline{o_{11}}}\right)_{ln} B_n+\left(\underline{\underline{o_{12}}}\right)_{ln} B_n'; & o_l' &= \left(\underline{\underline{o_{21}}}\right)_{ln} B_n+\left(\underline{\underline{o_{22}}}\right)_{ln} B_n';\\
p_l &= \left(\underline{\underline{p_{11}}}\right)_{ln} C_n+\left(\underline{\underline{p_{12}}}\right)_{ln} C_n'; & p_l' &= \left(\underline{\underline{p_{21}}}\right)_{ln} C_n+\left(\underline{\underline{p_{22}}}\right)_{ln} C_n';\\
q_l &= \left(\underline{\underline{q_{11}}}\right)_{ln} D_n+\left(\underline{\underline{q_{12}}}\right)_{ln} D_n'; & q_l' &= \left(\underline{\underline{q_{21}}}\right)_{ln} D_n+\left(\underline{\underline{q_{22}}}\right)_{ln} D_n';\\
r_l &= \left(\underline{\underline{r_{11}}}\right)_{ln} B_n+\left(\underline{\underline{r_{12}}}\right)_{ln} B_n'; & r_l' &= \left(\underline{\underline{r_{21}}}\right)_{ln} B_n+\left(\underline{\underline{r_{22}}}\right)_{ln} B_n';\\
s_l &= \left(\underline{\underline{s_{11}}}\right)_{ln} C_n+\left(\underline{\underline{s_{12}}}\right)_{ln} C_n'; & s_l' &= \left(\underline{\underline{s_{21}}}\right)_{ln} C_n+\left(\underline{\underline{s_{22}}}\right)_{ln} C_n';\\
t_l &= \left(\underline{\underline{t_{11}}}\right)_{ln} D_n+\left(\underline{\underline{t_{12}}}\right)_{ln} D_n'; & t_l' &= \left(\underline{\underline{t_{21}}}\right)_{ln} D_n+\left(\underline{\underline{t_{22}}}\right)_{ln} D_n'.
\end{aligned}$$

The elements of the matrices $\underline{\underline{e_{11}}}, \underline{\underline{e_{12}}}, \ldots, \underline{\underline{t_{22}}}$ are the integrals of the corresponding modal functions for stresses along the borehole boundary.

Least Squares Solution by Reichel et al. Algorithm

In the mode-matching method, a least square formalism is used to match the boundary conditions between solution regimes, whereby the coefficients in the expansion in terms of modal solutions are uniquely determined. To this end, we define the mean square errors on the boundary as

$$\mathcal{E}(u_n) = ||u_n^{(f)}(r^-,\theta) - u_n^{(s)}(r^+,\theta) - u_n^{(i)}(r^+,\theta)||^2, \tag{9a}$$

$$\mathcal{E}(\sigma_{nn}) = ||-p^{(f)}(r^-,\theta) - \sigma_{nn}^{(s)}(r^+,\theta) - \sigma_{nn}^{(i)}(r^+,\theta)||^2, \tag{9b}$$

$$\mathcal{E}(\sigma_{nb}) = ||-\sigma_{nb}^{(s)}(r^+,\theta) - \sigma_{nb}^{(i)}(r^+,\theta)||^2, \tag{9c}$$

$$\mathcal{E}(\sigma_{nz}) = ||-\sigma_{nz}^{(s)}(r^+,\theta) - \sigma_{nz}^{(i)}(r^+,\theta)||^2, \tag{9d}$$

where

$$||f||^2 = \oint_\Gamma \overline{f(s)}\, f(s)\, ds = \int_0^{2\pi} \overline{f(r(\theta))}\, f(r(\theta))\, r(\theta)\, d\theta$$

defines the norm of a square integrable function $f(\cdot)$ on the boundary. Notice that, in the above definition, the borehole radius is included as a positive weighting function. $\mathcal{E}(u_n)$ is the misfit of the normal displacement on the boundary, $\mathcal{E}(\sigma_{nn})$ is that of the normal stress, and $\mathcal{E}(\sigma_{nb})$ and $\mathcal{E}(\sigma_{nz})$ are those of the two tangential stresses. The objective is to find appropriate coefficients to minimize all these errors simultaneously[3].

We substitute the expressions in equations (4.6) through (4.8) into equations (9a)–(9d). For example, we calculate the mean square error of the normal displacement in equation (9a) and compare it with the minimization problem discussed in Appendix B. We found that the Reichel et al. algorithm (for least square approximations by trigonometric polynomials) can be employed to compute rapidly and accurately the coefficients $\{a_l, a_l', b_l, b_l', \ldots t_l, t_l'\}_{l=0}^{L}$, where L is the order of truncation. We have assumed that the displacement and stresses of the incident wave fields are known on the boundary at a set of distinct sample points. The weights in the Reichel et al. algorithm are chosen as $w_k = r_k$, corresponding to the radius of the irregular borehole at $\theta = \theta_k$.

Given that $\{a_l, a_l', b_l, b_l', \ldots t_l, t_l'\}_{l=0}^{L}$ are known, the coefficients $\{A_n, A_n', B_n, B_n', C_n, C_n', D_n, D_n'\}_{n=0}^{N}$ can then be determined uniquely by solving a (8N + 4)×(8N + 4) matrix equation[4] derived from the relationships given in section 2.2, where $N = L$ are the orders of truncation.

The truncation order is chosen such that the errors in equations (9a)–(9d) are much smaller than the norms of the incident wave field (relative error $< 10^{-4}$). This guarantees at least four digits of accuracy in the solution. The relative error is dependent on the shape of the borehole, i.e., the spectrum of the borehole cross-section in equation (1). Using double precision computations, we found that the relative error was less

[3]In the case of a circular borehole, i.e., $r(\theta) \equiv r_0$, these errors are minimal if and only if all the individual modes satisfy the boundary conditions themselves. This is due to the orthogonality of the modal functions. In this case, the mode-matching method reduces to the method we have developed in Schoenberg (1986) and Peng et al. (1993).

[4]The total number of unknown coefficients is 8 ×N +4, where the 4 is due to the property that $A_0' = B_0' = C_0' = D_0 \equiv 0$

than 10^{-14} for a circular borehole and less than 10^{-9} for an elliptical borehole, where $L = N = 10$ was used.

Given the error bounds on the boundary, we can show that the error at any point away from the boundary is also bounded with

$$|\mathbf{u}_N(\vec{r}) - \mathbf{u}(\vec{r})|^2 \leq M(\Omega)\, \mathcal{E}(u_n), \tag{10}$$

where $M(\Omega)$ is a positive constant independent of both N (the order of truncation) and position $\vec{r} \in \Omega$. Here $\mathbf{u}_N$ is the calculated displacement by the mode-matching method, and $\mathbf{u}$ is the exact solution. The proof is straight forward by taking account of the decaying nature of the Hankel functions at large distances.

Implementation

Several issues are of concern in the implementation of this technique. The most important one is the control of accuracy. The sources of inaccuracy may come from the singularity of the coefficient matrix, causing energy to leak between modes, or from the loss of significant digits in the evaluation of the Bessel functions $J_n(z) \to 0$ and the Hankel functions $H_n^{(1)}(z) \to \infty$ as $|z| \to 0$ and n large, or from the fact that the borehole cross-section may be so rough that more terms in the summations would be needed. In our experience, proper scaling and preconditioning can greatly improve the condition of the matrix equation. The method we have used to compute the Bessel and Hankel functions (adapted from du Toit, 1990) is accurate enough for any order and any complex argument.

Discretization along the borehole boundary also has some effects on accuracy. A denser discretization is needed at sharp corners, while in flat regions only sparse sampling is necessary. The automatic discretization scheme we use is based on the local curvature along the boundary. It is combined with the requirement that the size of the largest element be less than 1/25 of the shortest wavelength. The local curvature in polar coordinates is given by

$$\kappa = \frac{r^2 + 2\,(dr/d\theta)^2 - r\; d^2r/d\theta^2}{(r^2 + (dr/d\theta)^2)^{3/2}}. \tag{11}$$

In our calculations, the number of samples along the borehole boundary is 180, roughly in two degree intervals between two successive sampling points.

For a fixed discretization of the boundary, say, 180 elements or grid points, we compare the boundary integral method against the mode-matching method. The boundary integral method used in Randall (1991a, 1991b) has $J = 4{\times}180 = 720$ unknowns to be determined. This requires arithmetic operations on the order of $O(J^2)$ to solve the matrix equation alone, not including calculations for forming the coefficient matrices. The mode matching method developed here only needs arithmetic operations on the order of $O(J/4{\times}(8N + 4)) = O(J)$, where $N = 10$ is the order of truncation. This makes the mode-matching method a practical tool of computing synthetic seismograms in an irregular borehole, where the calculation is repeated for many samples in both frequency and vertical wavenumber.

APPLICATIONS TO BOREHOLE COUPLING

Case of an Elliptical Borehole

Boreholes with 10% ellipticity are not uncommon. Figure 2 shows a borehole cross section whose shape was determined with a borehole televiewer (Ellefsen, 1991). The major axis of the borehole is 19.1 cm in diameter; the minor one is 16.9 cm in diameter. The borehole is discretized with 180 elements where the boundary conditions are satisfied in the least square sense. In the following examples, the frequency of the incident wave is 1000 Hz. The formation is Berea sandstone. The fluid is ideal water. The order of truncation is $N = L = 10$.

Figure 3 shows the relative error in satisfying the boundary condition as a function of angle of incidence. The error is computed according to

$$E = \frac{||\sigma_{nn}^{(f)}(r^-, \theta) - \sigma_{nn}^{(s)}(r^+, \theta) - \sigma_{nn}^{(i)}(r^+, \theta)||}{||\sigma_{nn}^{(i)}(r^+, \theta)||}, \tag{12}$$

where the norm was defined in section 2.3. For a computation with double precision, this error is on the order of 10^{-9} for this particular example. This result implies that at least 8 significant digits are obtained in the solution. Surprisingly, the relative error increases with the increase of the angle of incidence (from 10^{-12} at grazing incidence to 6×10^{-9} at normal incidence). This behavior originates from approximating plane waves by superposition of finite sets of cylindrical waves.

Another way to demonstrate the accuracy of the mode-matching method is to examine the decay of the coefficients in the expansions (2a)-(2d), or in other words, to evaluate the contributions of higher order modes to the summations. Figure 4 is a barplot of magnitudes of coefficients $\{A_n, B_n, C_n, D_n\}_{n=0}^{n=N}$ as a function of harmonic order n. Shown here are the first 12 modes. The vertical axis (magnitude) is in a logarithmic scale. It is evident that the decay of $\{B_n, C_n, D_n\}$ is faster than exponential, implying that very few terms are actually contributing to the summation, the higher order terms are negligible. The coefficient $\{A_n\}$ fluctuates at the beginning and decays later as the order increases. Recall that $\{A_n\}$ is always associated with $J_n(z)$, while the others are associated with $H_n^{(1)}(z)$, where $z = O(0.1)$. Taking this into account, we have found that only the first 7 modes are significant.

Figure 5 shows the pressure at the center of the fluid as a function of angle of incidence. The incident wave is a plane compressional wave. The pressure is scaled by $P_0 = -\rho\alpha\omega^2$. Three calculations are shown in this figure. The solid line is the result for an equivalent circular borehole, the long dashed line shows the case where the P-wave incidents along the minor axis, and the short dashed line shows the case where the P-wave travels along the major axis. The pressure in the fluid is greater than that in an equivalent circular borehole when the incident P-wave is parallel to the minor axis; it is smaller when the incident P-wave is parallel to the major axis. The difference is about 10% at normal incidence, which is of the same order as the borehole ellipticity. At grazing incidence, these three curves converge, showing that a P-wave propagating in the vertical direction cannot 'see' the geometry of the fluid-filled borehole at all.

Figure 6 shows the pressure at the center of the fluid for a plane SV-wave incidence. The notations are the same as those in Figure 5. Again, the pressure in the fluid is larger when the incident SV-wave is parallel to the minor axis, and smaller when the incident SV-wave is parallel to the major axis. The difference is on the same order as the borehole ellipticity.

An explanation for these observations is that the elliptical borehole is stiffer against deformation along the minor axis than along the major axis. This has been shown in Randall's analysis (Randall, 1991b). He found that the phase velocity of the odd dipole (polarized in the direction of the minor axis) is larger than that of the even dipole (polarized in the direction of the major axis).

The solid motion in the formation, however, is affected less by the irregularity of the fluid-solid boundary. Figure 7 shows both the horizontal and vertical components of the solid displacement on the borehole wall at an azimuthal angle $\theta = 0^o$ (measured from the major axis). The displacements are scaled by the total displacement of the incident P-wave. Obviously, the dependence of the solid motion on the direction of the incident wave is insignificant compared to the effect on the pressure in the fluid. This observation is also true for a plane SV-wave incidence.

Other Borehole Cross-sections

Figure 8 shows a borehole cross-section without a symmetry axis. The dashed line is its equivalent circular borehole (in the sense of equal surface area). We compute only the pressure at the center of the fluid (as marked by the solid dot in this figure) for waves coming from various directions, since the effect of irregularities on the solid displacement is insignificant in the frequency range we are interested in.

Figure 9 shows the pressure at the center of the fluid as a function of angle of incidence. The incident wave is a plane P-wave and the formation is Berea sandstone. A total of 8 curves are shown for the azimuth of the incident wave ranging from 0^o to 360^o at 45^o intervals. The pressure is scaled by P_0. As expected, the pressure in the fluid increases with the increase of the angle of incidence. However, the curves split into two branches depending on the azimuthal angle of the incident wave. A closer analysis shows that the curves labeled as $45^o, 90^o$ and 225^o belong to a cluster with smaller amplitudes, while the rest are in another cluster with larger amplitudes. The explanation is as follows. Independent of the irregularity of the borehole, the dipole motion tends to split into two and only two branches with the faster one polarized along the effective minor axis and the slower one along the effective major axis. The predominant contribution to the pressure in the fluid comes from the monopole and dipole components of the incident wave, and the reminder are negligible.

Figure 10 shows the same calculation as Figure 9 but for a plane SV-wave incidence. The pressure shows a lobe around 45^o incidence. Again, the pressure in the fluid splits into two branches depending on the azimuthal angle of the incident wave. The one closer to the effective minor axis of the irregular borehole tends to generate larger pressure in the fluid; the one closer to the effective major axis tends to induce smaller pressure.

APPLICATIONS TO ACOUSTICAL WELL LOGGING

The mode-matching method developed in this paper can also be applied to sonic logging problems where one is interested in the effects of borehole irregularity on multipole (especially dipole) logging seismograms. Among the possible effects is the mode splitting (or cross-mode coupling) in an irregular borehole, a phenomenon that could also be attributed to formation anisotropy (Hatchell and Cowles, 1992).

A Circular Borehole

Sonic logging in a circular borehole is a subject of intensive studies (among others, Cheng and Toksöz, 1981; Toksöz et al., 1984). We compute synthetic dipole seismograms for a dipole source in a circular borehole using both the mode-matching and the discrete wavenumber methods (see Schmitt et al., 1988 for the latter method). Our objective is to compare the results of the two methods. This serves as an accuracy test for the application of the mode-matching method to sonic well logging problems. We use a model where the borehole is circular in cross-section, the radius is 0.1016 m, and the well is filled with fresh water. The formation is homogeneous with compressional velocity 3464 m/s, shear velocity 2000 m/s, and density 2.0 g/cm^3. A dipole source is at the borehole center. The dipole receivers are evenly distributed at offsets between 1.0 m and 4.3 m from the source. Both the source and the receivers are polarized in the same direction. The source time history is a Ricker wavelet with the central frequency of 2500 Hz. Figure 11 shows the resulting synthetic seismograms. The solid lines in this figure are the dipole seismograms computed by the mode-matching method; the dashed lines are those by the discrete wavenumber method. The agreement between these two methods is remarkable, although the amplitudes at far offsets differ slightly.

An Elliptical Borehole

In the following examples, we use the elliptical borehole shown in Figure 2. The array of receivers is located at offsets between 1.0 m and 3.2 m from the source. The source time function is a Ricker wavelet. The central frequency is 4000 Hz. The formation is Berea sandstone.

In the first two examples, we use a monopole source and an array of dipole receivers whose orientation is in the direction of either the major axis (Figure 12) or the minor axis (Figure 13). The seismograms are evaluated slightly off-axis since the displacement at the absolute center of the borehole is zero because of symmetry considerations. In both figures, a low frequency event of large amplitude is clearly visible in the dipole waveform. Surprisingly, it travels with the phase velocity of the tube wave, suggesting that it is generated by the cross-mode coupling between the propagating tube wave and the dipole motion in the presence of borehole ellipticity. The dispersive wave trains surrounding this tube-wave-like event have the characteristics of the dipole waveform, and are generated by the tube wave continuously along its path of propagation. At low frequencies, the dipole motion has the phase speed of the formation shear velocity.

At high frequencies, it travels much slower than the formation shear speed. Close comparisons also reveal that the phase velocity of the dipole wave in Figure 13 (polarized along the minor axis) is larger than that in Figure 12 (polarized along the major axis). This result is in agreement with the theoretical prediction by Randall (1991a). The amplitude of the seismogram in Figure 13 is about 18% larger than that in Figure 12. Recall that the borehole ellipticity in these examples is about 10%. This observation seems to suggest that, for an elliptical borehole, differences in the excitation of the two perpendicularly polarized dipole modes by a monopole source are of the same order as the borehole ellipticity.

In the next two examples we use a dipole source and an array of monopole receivers. The source polarization is in the direction of either the major axis (Figure 14) or the minor axis (Figure 15). Instead of observing tube waves in the monopole seismograms, one sees a dispersive wave train with characteristics of a dipole motion. It is generated by a cross-mode coupling between the traveling dipole energy and the monopole motion at the receiver location. As expected, the phase velocity at high frequencies is larger in Figure 15 (polarized along the minor axis) than in Figure 14 (polarized along the major axis).

In summary, the synthetic examples in this section show that in an elliptical borehole the cross-mode coupling phenomena are evident in sonic logging seismograms using both monopole and multipole tools. Depending on the orientation of the dipole source or dipole receivers, the difference in the phase velocities of the dipole flexural waves at high frequencies and the excitations of the cross-modes are of the same order as the borehole ellipticity.

DISCUSSIONS AND CONCLUSIONS

In this paper, we have presented a mode-matching method to compute the pressure in the fluid and the solid displacement in the formation for an elastic wave impinging upon an irregular borehole. In this method, the wave fields in both the fluid and the formation are expressed as a finite summation of mode solutions. The unknown coefficients are determined by satisfying the boundary conditions at the fluid-solid interface in a least square sense. The Reichel et al. (1991) algorithm is incorporated into the formulation, achieving both accuracy and computational speed. This technique requires arithmetic operations on the order of $O(J)$ as compared to the boundary integral equation method which needs $O(J^2)$ arithmetic operations (J is the number of discrete samples on the boundary). For a circular borehole, this method reduces exactly to the one given in Chapter 2. For a borehole of any other cross-section, the relative errors in satisfying the boundary conditions are found to be negligible (of course, it is dependent on the order of truncation).

The method has also been applied to compute the synthetic sonic logs in a borehole of elliptical cross-section. Several examples have been given to demonstrate the cross-mode coupling phenomena. A monopole source excites dipole motions whose propagational properties are similar to tube waves, and a dipole source excites monopole motions

whose propagational properties are similar to flexural waves.

In summary, we draw the following conclusions:

- The pressure in the fluid is sensitive to the irregularity of the borehole cross-section, while the solid displacement in the formation is less affected.
- For both P-wave and S-wave incidences, the pressure in an elliptical borehole is larger than the pressure in an equivalent circular borehole if the incident wave is along the minor axis. It is smaller than that in an equivalent circular borehole if the incident wave is along the major axis. The relative difference in the amplitudes of the pressures is on the same order as the borehole ellipticity.
- In a borehole of arbitrary cross-section, the pressure in the fluid splits into two distinct branches depending on the azimuthal angles of the incident P- and S-waves. The larger branch is associated with incident waves close to the minor axis, while the smaller branch is associated with those near the major axis.
- In an elliptical borehole, a centered monopole source excites dipole motions in the borehole fluid whose characteristics are similar to tube waves. A centered dipole source excites monopole motions whose characteristics are similar to flexural waves.

ACKNOWLEDGEMENTS

This work is supported by the Borehole Acoustics and Logging Consortium at M.I.T.

REFERENCES

Cheng, C.H., and M.N. Toksöz, 1981, Elastic wave propagation in a fluid-filled borehole and synthetic acoustic logs, *Geophysics, 46,* 1042–1053.

Dart, R.L., and M.L. Zoback, 1989, Wellbore breakout stress analysis within the central and eastern continental United States, *The Log Analyst, 30,* 12–25.

Du Toit, C.F., 1990, The numerical computation of Bessel functions of the first and second kind for integer orders and complex arguments, *IEEE Trans. Antenna and Propagation, 38,* 1341–1349.

Ellefsen, K.J., 1990, *Elastic wave propagation along a borehole in an anisotropic medium,* PhD thesis, M.I.T., Cambridge, Massachusetts.

Hatchell, P.J., and C.S. Cowles, 1992, Flexural borehole modes and measurement of shear-wave azimuthal anisotropy, in *62nd Ann. Internat. Mtg., Soc. Expl. Geophys., Expanded abstracts,* 201–204.

Hilchie, D.W., 1968, Caliper logging–theory and practice, *The Log Analyst, 9,* 3–12.

Liu, H., and C.J. Randall, 1991, Synthetic waveforms in noncircular boreholes using a boundary integral equation method, in *61sth Ann. Internat. Mtg., Soc. Expl. Geophys., Expanded Abstracts,* 843–845.

Norris, A., 1990, The speed of a tube wave, *J. Acoust. Soc. Am., 87,* 414–417.

Okuno, Y., 1990, The mode-matching method, in *Analysis Methods for Electromagnetic Wave Propagation,* edited by Yamashita, E., Artech House Inc., Norwood, Massachusetts.

Randall, C.J., 1991a, Modes of noncircular fluid-filled boreholes in elastic formations, *J. Acoust. Soc. Am., 89,* 1002–1016.

Randall, C.J., 1991b, Multiple acoustic waveforms in nonaxisymmetric boreholes and formations, *J. Acoust. Soc. Am., 90,* 1620–1631.

Reichel, L., G.S. Ammar, and W.B. Gragg, 1991, Discrete least squares approximation by trigonometric polynomials, *Math. Comp., 57,* 273–289.

Schoenberg, M., 1986, Fluid and solid motion in the neighborhood of a fluid-filled borehole due to the passage of a low frequency elastic plane wave, *Geophysics, 51,* 1191–1205.

Toksöz, M.N., C.H. Cheng, and M.E. Willis, 1984, Seismic waves in a borehole–a review, in *Vertical Seismic Profiling: 14B, M.N. Toksöz and R.R. Stewart (eds.),* 256–275, Geophysical Press.

Zimmerman, R.W., 1986, Compressibility of two-dimensional cavities of various shapes, *J. Appl. Mech., 108,* 500–504.

APPENDIX A: LISTS OF COEFFICIENTS

We list the coefficients of the stresses and displacements in the harmonic expansions as follows:

$$\mathcal{U}_n^{(f)}(r) = \alpha_f k_f J_n'(k_f r), \quad \mathcal{V}_n^{(f)}(r) = \alpha_f \tfrac{k_f}{k_f r} n J_n(k_f r), \quad \mathcal{W}_n^{(f)}(r) = \alpha_f i k_z J_n(k_f r)$$

$$\mathcal{U}_n^{(\phi)}(r) = \alpha k_p H_n^{(1)'}(k_p r), \quad \mathcal{U}_n^{(\xi)}(r) = -\beta \tfrac{k_z k_s}{k_\beta} H_n^{(1)'}(k_s r), \quad \mathcal{U}_n^{(\psi)}(r) = \beta \tfrac{k_s}{k_s r} n H_n^{(1)}(k_s r)$$

$$\mathcal{V}_n^{(\phi)}(r) = \alpha \tfrac{k_p}{k_p r} n H_n^{(1)}(k_p r), \quad \mathcal{V}_n^{(\xi)}(r) = -\beta \tfrac{k_z}{k_\beta r} n H_n^{(1)}(k_s r), \quad \mathcal{V}_n^{(\psi)}(r) = \beta k_s H_n^{(1)'}(k_s r)$$

$$\mathcal{W}_n^{(\phi)}(r) = \alpha i k_z H_n^{(1)}(k_p r), \quad \mathcal{W}_n^{(\xi)}(r) = \beta i \tfrac{k_s^2}{k_\beta} H_n^{(1)}(k_s r), \quad \mathcal{W}_n^{(\psi)}(r) = 0$$

$$\mathcal{R}_n^{(f)}(r) = -\rho_f \alpha_f \omega^2 J_n(k_f r)$$

$$\mathcal{R}_n^{(\phi)}(r) = -\rho\alpha[(\omega^2 - 2\beta^2 k_z^2) H_n^{(1)}(k_p r) + \tfrac{2\beta^2 k_p^2}{k_p r}(H_n^{(1)'}(k_p r) - \tfrac{n^2}{k_p r} H_n^{(1)}(k_p r))]$$

$$\mathcal{R}_n^{(\xi)}(r) = 2\rho\beta^3 \tfrac{k_z k_s^2}{k_\beta}[H_n^{(1)}(k_s r) + \tfrac{1}{k_s r} H_n^{(1)'}(k_s r) - \tfrac{n^2}{k_s^2 r^2} H_n^{(1)}(k_s r)]$$

$$\mathcal{R}_n^{(\psi)}(r) = -2\rho\beta^3 k_s^2 n[\tfrac{1}{k_s^2 r^2} H_n^{(1)}(k_s r) - \tfrac{1}{k_s r} H_n^{(1)'}(k_s r)]$$

$$\mathcal{T}_n^{(\phi)}(r) = -2\rho\alpha\beta^2 k_p^2 n[\tfrac{1}{k_p^2 r^2} H_n^{(1)}(k_p r) - \tfrac{1}{k_p r} H_n^{(1)'}(k_p r)]$$

$$\mathcal{T}_n^{(\xi)}(r) = 2\rho\beta^3 \tfrac{k_z k_s^2}{k_\beta} n[\tfrac{1}{k_s^2 r^2} H_n^{(1)}(k_s r) - \tfrac{1}{k_s r} H_n^{(1)'}(k_s r)]$$

$$\mathcal{T}_n^{(\psi)}(r) = -\rho\beta^3 k_s^2[H_n^{(1)}(k_s r) + \tfrac{2}{k_s r} H_n^{(1)'}(k_s r) - \tfrac{2n^2}{k_s^2 r^2} H_n^{(1)}(k_s r)]$$

$$\mathcal{Z}_n^{(\phi)}(r) = 2i\rho\alpha\beta^2 k_z k_p H_n^{(1)'}(k_p r)$$

$$\mathcal{Z}_n^{(\xi)}(r) = -i\rho\beta^3 \tfrac{(k_z^2 - k_s^2) k_s}{k_\beta} H_n^{(1)'}(k_s r)$$

$$\mathcal{Z}_n^{(\psi)}(r) = i\rho\beta^3 k_z \tfrac{k_s}{k_s r} n H_n^{(1)}(k_s r)$$

$$\mathcal{L}_n^{(\phi)}(r) = -\rho\alpha[\omega^2 - 2\beta^2({k_\alpha}^2 - k_z^2)] H_n^{(1)}(k_p r)$$

$$\mathcal{L}_n^{(\xi)}(r) = -2\rho\beta^3 \tfrac{k_z}{k_\beta}({k_\beta}^2 - k_z^2) H_n^{(1)}(k_s r)$$

$$\mathcal{L}_n^{(\psi)}(r) = 0$$

$$\mathcal{M}_n^{(\phi)}(r) = -\rho\alpha[(\alpha^2 - 2\beta^2){k_\alpha}^2 H_n^{(1)}(k_p r) - 2\beta^2 \tfrac{k_p^2}{k_p r} H_n^{(1)'}(k_p r) + 2\beta^2 \tfrac{k_p^2}{k_p^2 r^2} n^2 H_n^{(1)}(k_p r)]$$

$$\mathcal{M}_n^{(\xi)}(r) = -2\rho\beta^3 \tfrac{k_z}{k_\beta}[\tfrac{k_s^2}{k_s r} H_n^{(1)'}(k_s r) - \tfrac{k_s^2}{k_s^2 r^2} n^2 H_n^{(1)}(k_s r)]$$

$$\mathcal{M}_n^{(\psi)}(r) = 2\rho\beta^3 k_s^2 n[\tfrac{1}{k_s^2 r^2} H_n^{(1)}(k_s r) - \tfrac{1}{k_s r} H_n^{(1)'}(k_s r)]$$

$$\mathcal{N}_n^{(\phi)}(r) = 2i\rho\alpha\beta^2 \tfrac{k_z k_p}{k_p r} n H_n^{(1)}(k_p r)$$

$$\mathcal{N}_n^{(\xi)}(r) = i\rho\beta^3 \tfrac{{k_\beta}^2 - 2k_z^2}{k_s r} \tfrac{k_s}{k_\beta} n H_n^{(1)}(k_s r)$$

$$\mathcal{N}_n^{(\psi)}(r) = i\rho\beta^3 k_z k_s H_n^{(1)'}(k_s r)$$

where, as a reminder, $k_\alpha = \frac{\omega}{\alpha}$, $k_\beta = \frac{\omega}{\beta}$, $k_p = \sqrt{{k_\alpha}^2 - k_z^2}$, $k_s = \sqrt{{k_\beta}^2 - k_z^2}$ and $k_f = \sqrt{\frac{\omega^2}{\alpha_f^2} - k_z^2}$. The vertical wavenumber $k_z = k_\alpha \cos\delta$ for plane P wave incidence and $k_z = k_\beta \cos\delta$ for plane shear wave incidence. δ is the angle of incidence.

APPENDIX B: DISCRETE LEAST SQUARES APPROXIMATION BY TRIGONOMETRIC POLYNOMIALS

This appendix summarizes an algorithm developed by Reichel et al. (1991) for the discrete least squares approximation of a real-valued function by trigonometric polynomials. The function values are given at arbitrary distinct nodes in the interval $[0, 2\pi)$. This algorithm has been employed to minimize the errors of satisfying the fluid-solid interface boundary conditions in a borehole of irregular shape.

This algorithm solves the following minimization problem

$$||f - t|| \equiv \left(\sum_{k=1}^{m} |f(\theta_k) - t(\theta_k)|^2 w_k^2 \right)^{1/2} = \text{minimum}\ , \qquad (\text{B}-1)$$

given a set of samples $\{f(\theta_k)\}_{k=1}^m$ of $f(\theta)$ at distinct nodes $\{\theta_k\}_{k=1}^m$ in the interval $[0, 2\pi)$. $\{w_k^2\}_{k=1}^m$ is a set of positive weights and

$$t(\theta) = a_0 + \sum_{j=1}^{l} (a_j \cos j\theta + b_j \sin j\theta), \quad a_j, b_j \in \mathbf{R}, \qquad (\text{B}-2)$$

is a trigonometric polynomial of order l. The problem is to find the coefficients $\{a_j, b_j\}_{j=0}^l$ such that the error in equation (B-1) is as small as possible[5].

Making the substitution $z = e^{i\theta}$ and noticing that equation (B-2) can be written as (Grenander and Szegö, 1984)

$$t(\theta) = z^{-l}\, p(z),$$

we can recast the minimization in equation (B-1) as

$$\left(\sum_{k=1}^{m} \overline{(g(z_k) - p(z_k))}\, (g(z_k) - p(z_k))\, w_k^2 \right)^{1/2} = \text{minimum}\ , \qquad (\text{B}-3)$$

where $g(z) = z^l f(\theta)$ is the known data, and $p(z) = \sum_{j=0}^{n-1} c_j z^j$ is a polynomial of degree n with $n = 2l + 1$. The coefficients $\{c_j\}_{j=0}^{n-1}$ are related to the coefficients $\{a_j, b_j\}_{j=0}^l$ by

$$\begin{cases} a_0 = c_l, \\ a_j = c_{l+j} + c_{l-j}, \\ b_j = i(c_{l+j} - c_{l-j}). \end{cases}$$

[5] if $w_k \equiv 1$ and $\{\theta_k\}_{k=1}^m$ are equally sampled between $[0, 2\pi)$, the Reichel et al. algorithm reduces to FFT (the fast Fourier transform).

Let $R = [r_{jk}]$ be an upper triangular matrix whose nontrivial elements are determined by

$$z^{k-1} = \sum_{j=1}^{k} r_{jk}\, \psi_{j-1}(z), \quad 1 \le k \le n \tag{B-4}$$

and let $Q = [q_{kj}]$ be a $m \times n$ matrix defined by

$$q_{kj} = \psi_j(z_k)\, w_k, \quad j = 0, ..., n-1;\ k = 1, ..., m \tag{B-5}$$

where $\{\psi_j\}_{j=0}^{m-1}$ is the family of *orthonormal* Szegö polynomials[6] with respect to the inner product defined by

$$< g, h > \equiv \sum_{k=1}^{m} \overline{g(z_k)}\, h(z_k)\, w_k^2.$$

The usefulness of the matrices R and Q becomes obvious if we write down the result

$$Q\, R\, \mathbf{c} = D\, \mathbf{g} \tag{B-6}$$

obtained by Reichel et al. (1991). Where $\mathbf{c} = [c_0, c_1, ..., c_{n-1}]^T \in \mathbf{C}^n$ is the coefficient vector solving equation (B-3), and $\mathbf{g} = [g(z_1), g(z_2), ..., g(z_m)]^T \in \mathbf{C}^m$ is the data vector. $D = diag[w_1, w_2, ..., w_m]$ is a diagonal matrix whose elements are the positive weights $\{w_k\}$. That matrix serves as a weighting factor or as the variance of the data.

This technique relies upon the speed and accuracy for computing Q^* and R^{-1}. The matrix Q, by definition, has orthonormal columns. That is, $Q^*Q = I$, where the superscript star denotes the Hermitian transpose. Q is obtained by simply evaluating the Szegö polynomials at the set of samples $\{z_k\}_{k=1}^{m}$; R^{-1} is composed of the coefficients of the Szegö polynomials in the power basis $\{1, z, z^2, ..., z^n\}$, and is obtained directly from the coefficients of the Szegö polynomials. The Szegö polynomials and its expansions on the power basis can be efficiently computed by making use of the Szegö recurrence relations. The scheme requires only $O(mn)$ arithmetic operations as compared to $O(mn^2)$ operations needed for other algorithms, where m is number of nodes (samples), n is the

[6]The Szegö polynomial $\psi_j(z)$ and its complementary polynomial $\widetilde{\psi_j}(z)$ satisfy the following Szegö recurrence relations (Reichel et al., 1991):

$$\psi_0(z) = \widetilde{\psi_0}(z) = 1/\sigma_0,$$

$$\sigma_{j+1}\, \psi_{j+1}(z) = z\psi_j(z) + \gamma_{j+1}\, \widetilde{\psi_j}(z),$$

$$\sigma_{j+1}\, \widetilde{\psi}_{j+1}(z) = z\overline{\gamma}_{j+1}\, \psi_j(z) + \widetilde{\psi_j}(z), \quad j = 0, 1, ..., n-2,$$

where the recurrence coefficients $\gamma_{j+1} \in \mathbf{C}$ and $\sigma_{j+1} > 0$ are determined by

$$\sigma_0 = \alpha_0 = \left(\sum_{k=1}^{m} w_k^2 \right)^{1/2},$$

$$\gamma_{j+1} = - < 1,\ z\psi_j(z) > / \alpha_j,$$

$$\sigma_{j+1} = (1 - |\gamma_{j+1}|^2)^{1/2},$$

$$\alpha_{j+1} = \alpha_j \sigma_{j+1}.$$

number of unknown coefficients. A detailed account of this technique can be found in algorithm 3.1 and algorithm 4.1 of Reichel et al. (1991).

The Szegö polynomials are dependent on the set of weights $\{w_k\}$ and the set of samples $\{z_k\}_{k=1}^{m}$ on the unit circle. The merit of the Reichel et al. algorithm is that the basis functions $\{\psi_j(z_k)\}_{j=1}^{n}$ are adaptive to the shape of the noncircular borehole. Figure 16 shows a representative Szegö polynomial $\psi_5(z)$ on the unit circle, using the elliptical borehole in Figure 2 and the discretization as marked in the figure. Recall that 180 elements are used in discretizing the borehole and the order of truncation is L =10. The Szegö polynomial is similar to a sinusoidal function. However, its amplitude is modulated by the shape of the borehole: it is larger near the minor axis and smaller near the major axis of the borehole. Although it is periodic with a 2π periodicity, the real part is not at a maximum and the imaginary part is not zero at $\theta = 0$, π, and 2π.

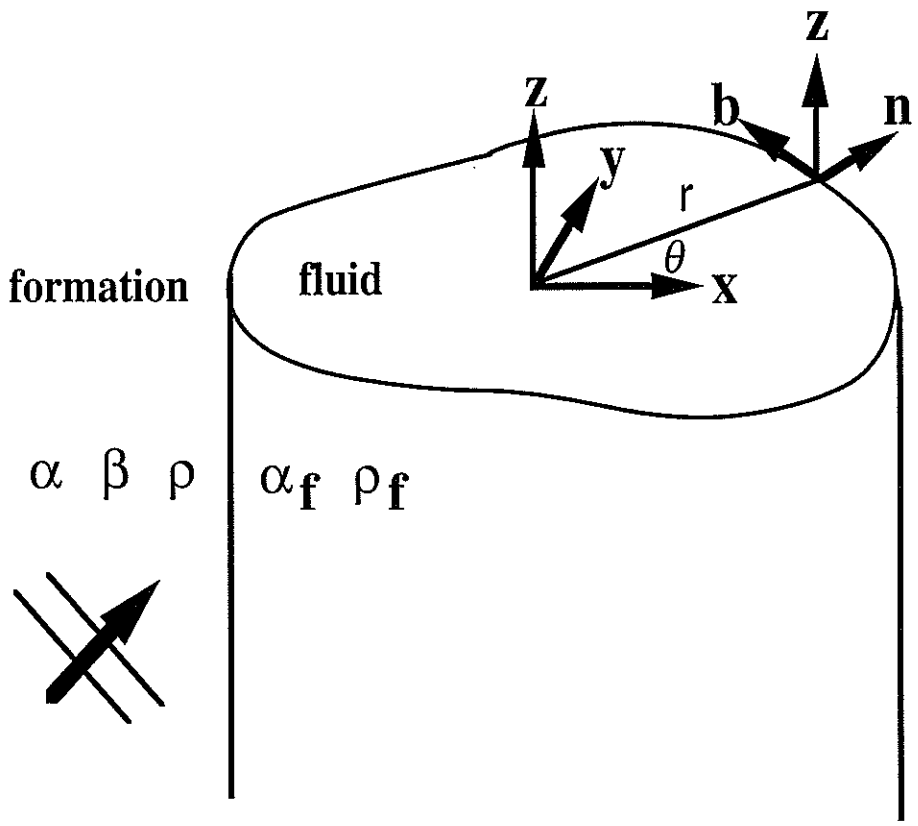

Figure 1: An irregular and fluid-filled borehole in a homogeneous and elastic formation. The fluid has a compressional velocity α_f and a density ρ_f. The formation has a compressional velocity α, a shear velocity β, and a density ρ. In this figure, $(\mathbf{r},\theta,\mathbf{z})$ is a cylindrical coordinate system; $(\mathbf{n},\mathbf{b},\mathbf{z})$ is a local orthogonal coordinate frame in which the boundary conditions between the fluid-solid interface are satisfied.

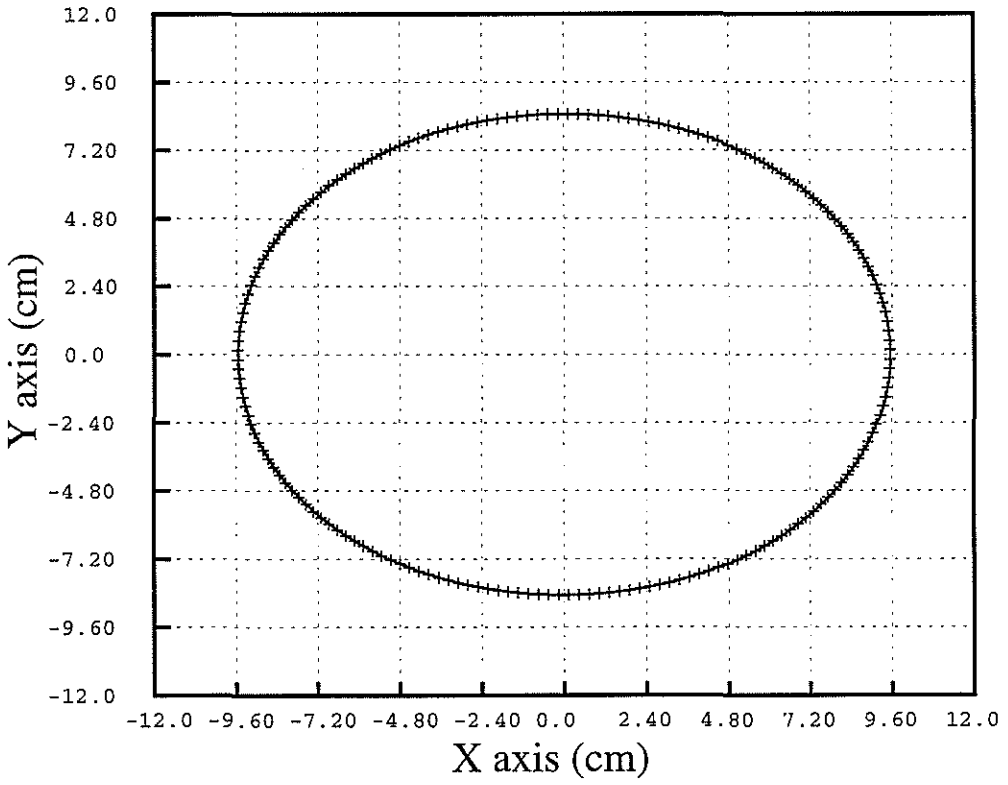

Figure 2: An elliptical borehole whose cross-section was determined with a downhole televiewer (adapted from Ellefsen, 1991). The major axis is 19.10 *cm*; the minor axis is 16.9 *cm*. The circumference of the borehole is divided into 180 elements.

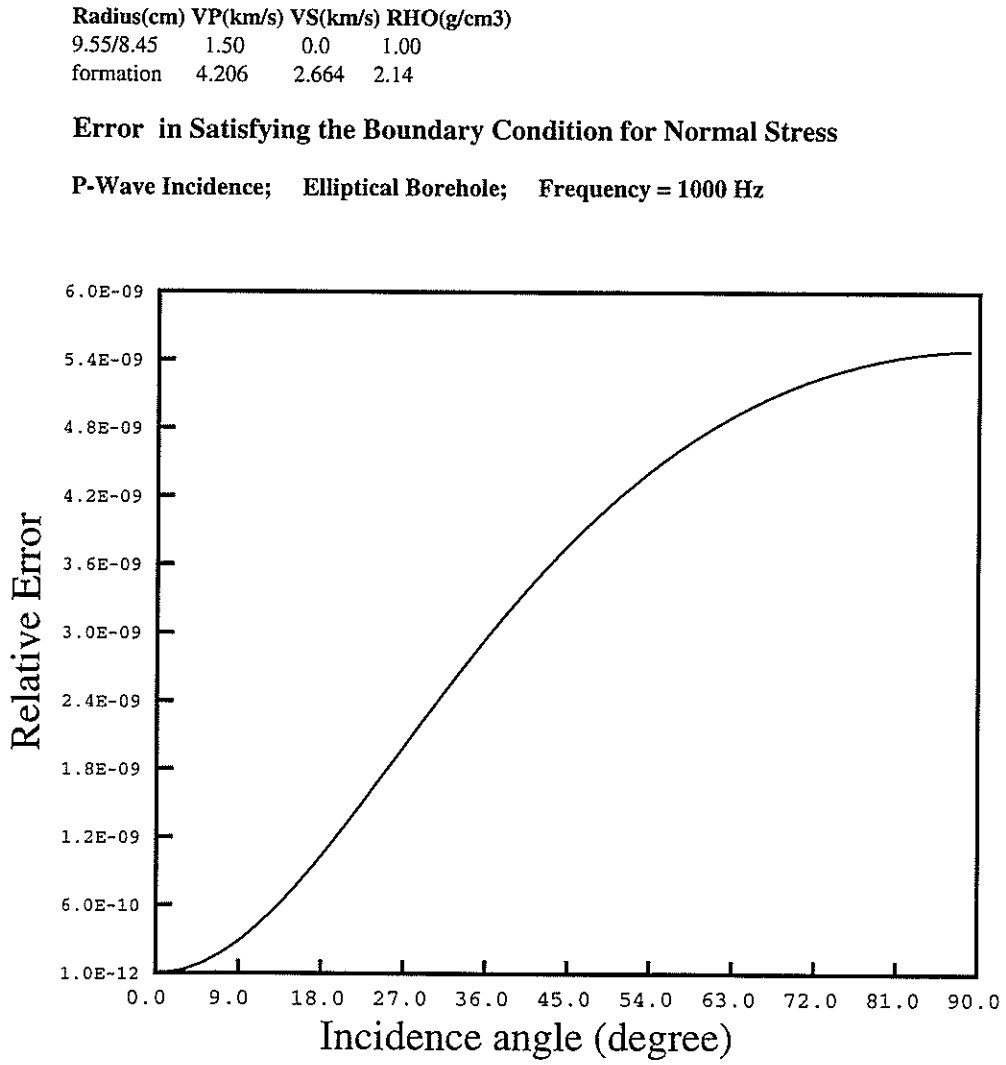

Figure 3: The relative error in satisfying the boundary condition as a function of angle of incidence. Shown is an example for the normal stress in the local coordinates (**n**,**b**,**z**) at the boundary. The borehole is shown in Figure 2. The horizontal axis is the angle of incidence. The vertical axis is the relative error in a logarithmic scale.

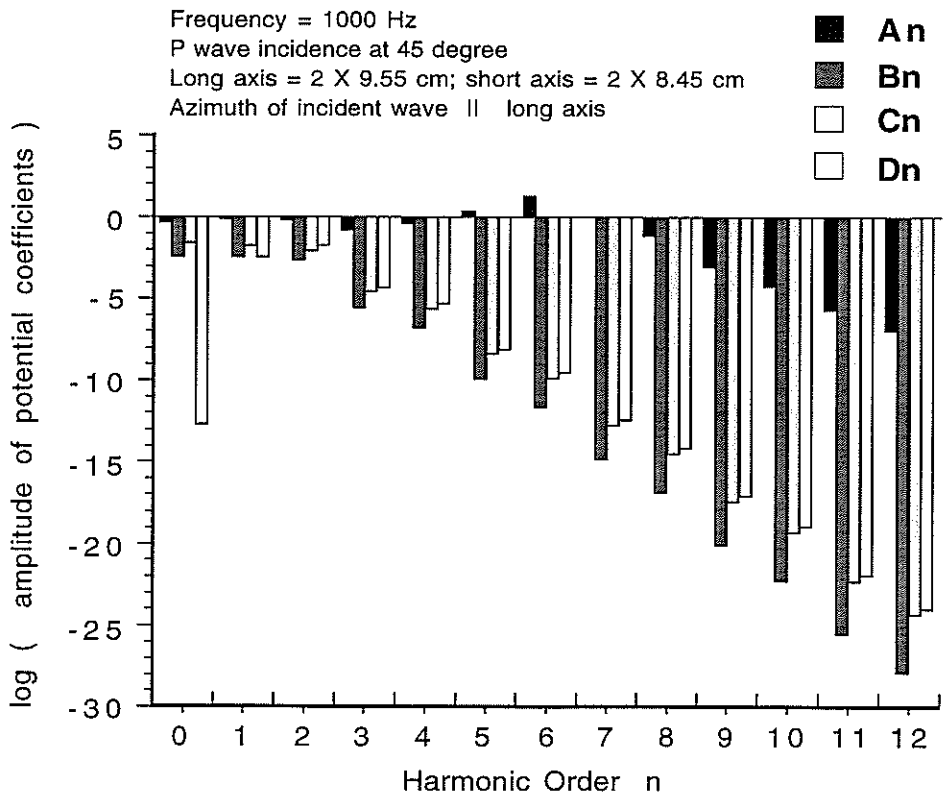

Figure 4: Magnitude of the coefficients $[A_n, B_n, C_n, D_n]_{n=0}^{n=N}$ in equations (2a)–(2d) at different harmonic orders n. The vertical axis is in a logarithmic scale. The calculation is done at a frequency of 1000 Hz and for a plane P-wave incidence at $\delta = 45^o$ with respect to the borehole axis. The borehole is shown in Figure 2.

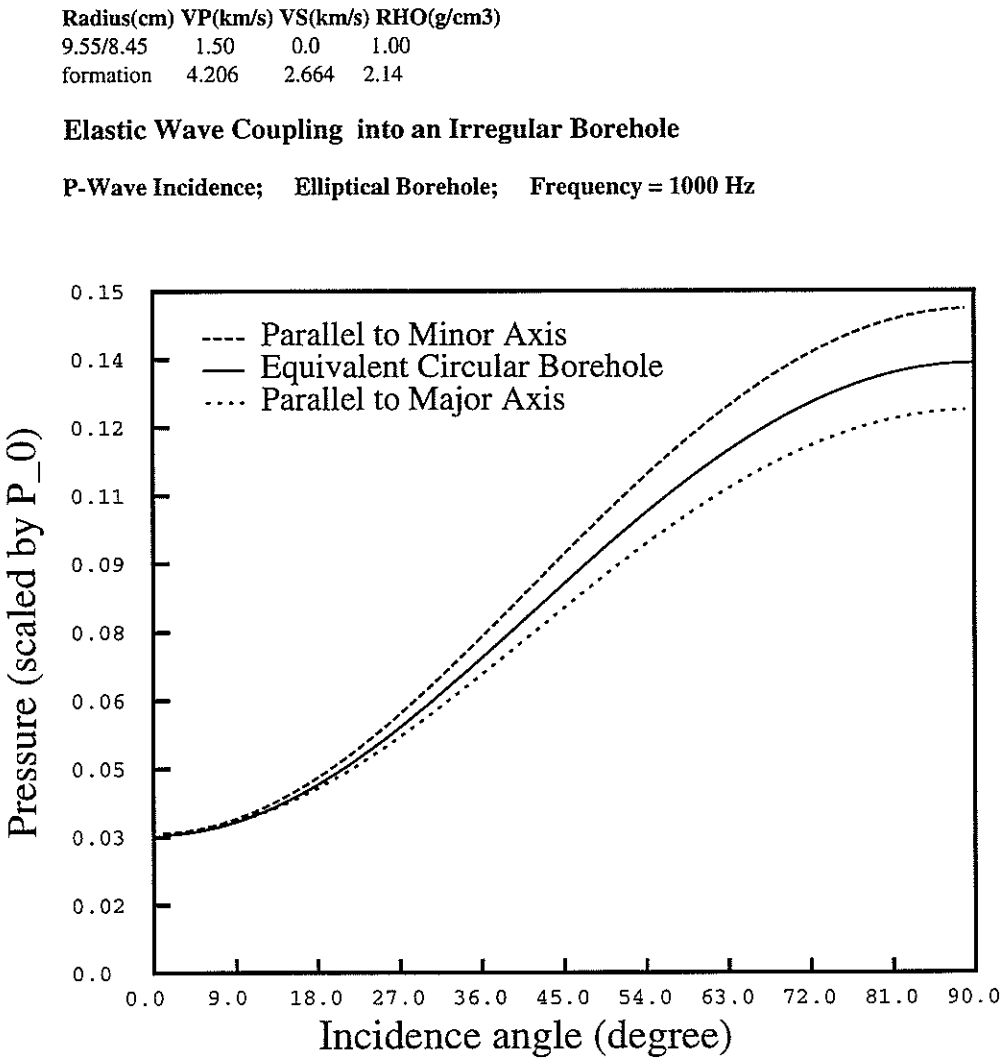

Figure 5: Pressure at the center of the fluid as a function of angle of incidence. The incident wave is a plane P-wave whose frequency is 1000 Hz. The formation is Berea sandstone. The pressure is scaled by the pressure of the incident P-wave. The solid line in this figure is the pressure in the fluid computed for an equivalent circular borehole. The line in long dashes is the pressure in the fluid for an incident P-wave propagating parallel to the minor axis. The line in short dashes is that for an incident P-wave propagating parallel to the major axis.

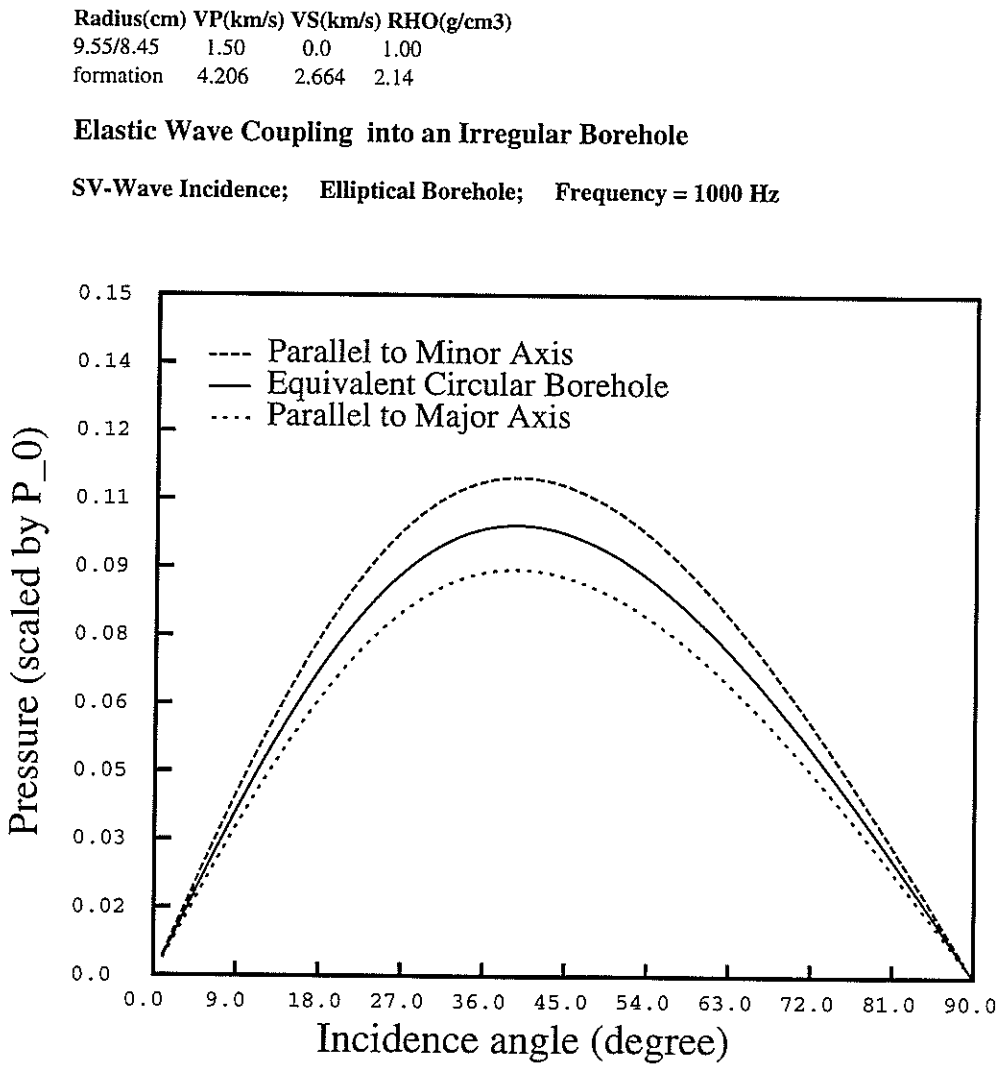

Figure 6: Pressure at the center of the fluid as a function of angle of incidence. The incident wave is a plane SV-wave whose frequency is 1000 Hz. The formation is Berea sandstone. The solid line in this figure is the pressure in the fluid computed for an equivalent circular borehole. The line in long dashes is the pressure in the fluid for an incident SV-wave propagating parallel to the minor axis. The line in short dashes is that for an incident SV-wave propagating parallel to the major axis.

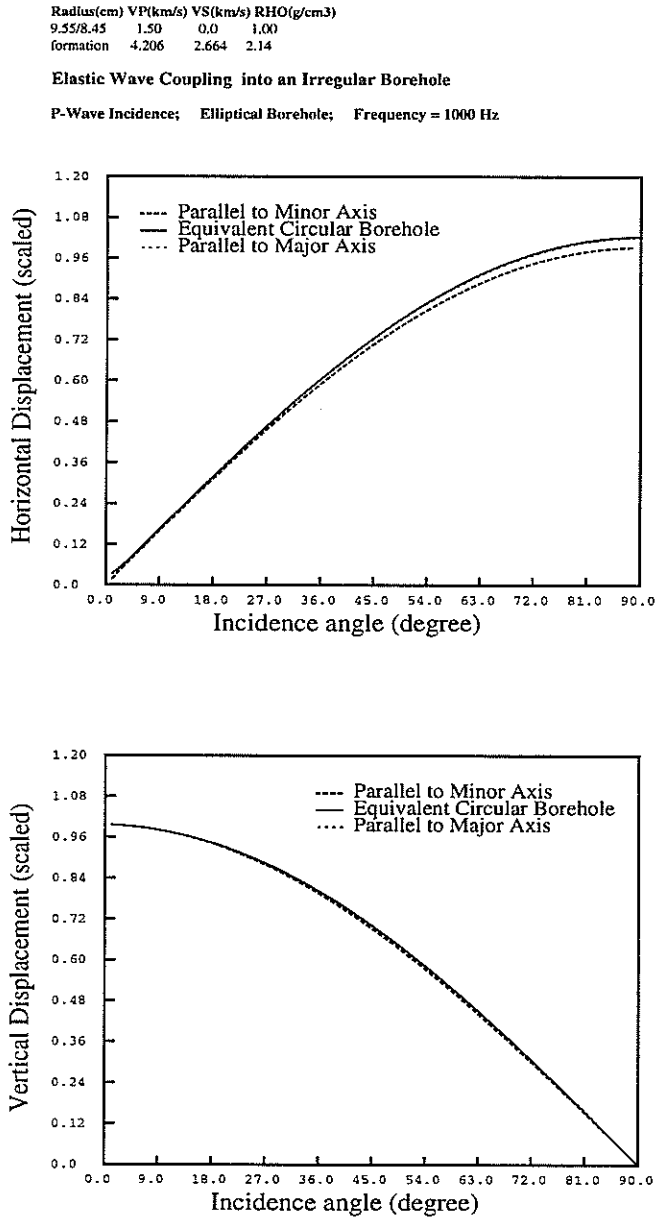

Figure 7: Horizontal (a) and vertical (b) components of the solid displacement at the borehole wall as a function of angle of incidence. The incident wave is a plane P-wave whose frequency is 1000 Hz. The formation is Berea sandstone. The borehole is elliptical. The displacements are scaled by the total displacement of the incident wave. The solid lines in these figures are the displacements in the formation computed for an equivalent circular borehole. The lines in long dashes are those for an incident P-wave propagating parallel to the minor axis. The lines in short dashes are those for an incident P-wave propagating parallel to the major axis.

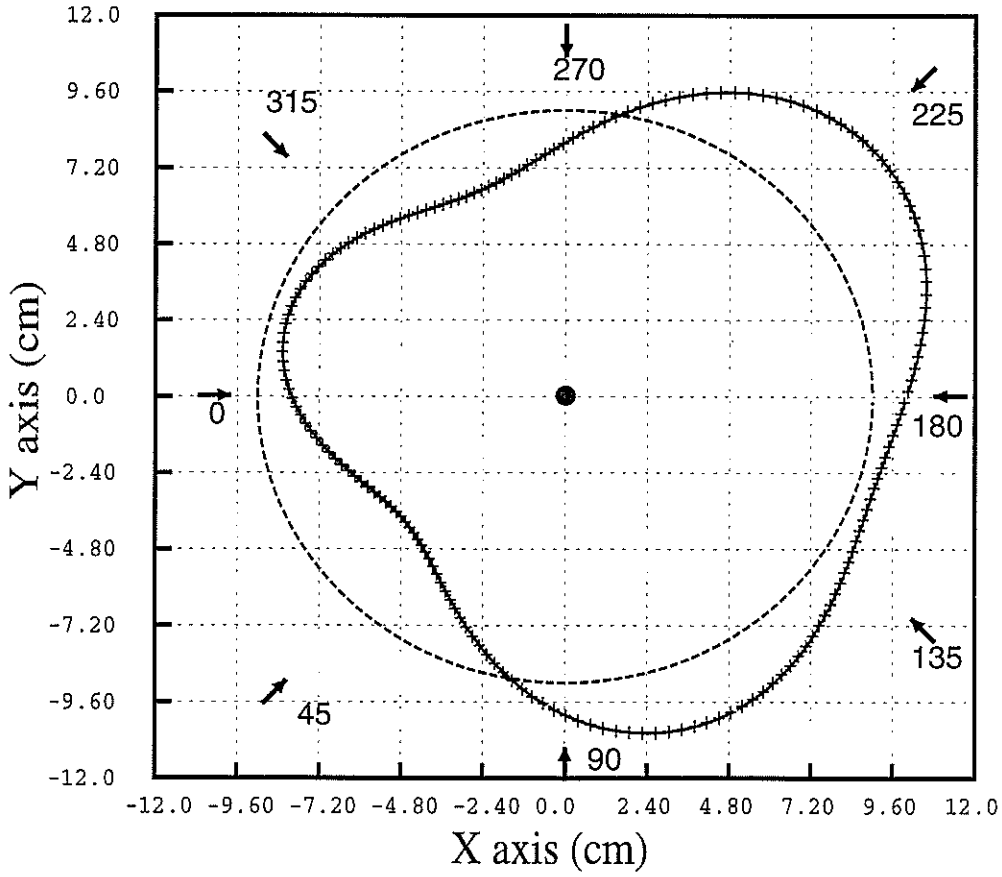

Figure 8: A borehole whose cross-section lacks any symmetry axis. The dashed circle in this figure is the equivalent circular borehole. The arrows are the azimuthal directions of the incident elastic wave in the formation. The dot at the center of the figure corresponds to the center of the borehole where the pressure in the fluid is computed. Also shown are 180 elements discretizing the circumference.

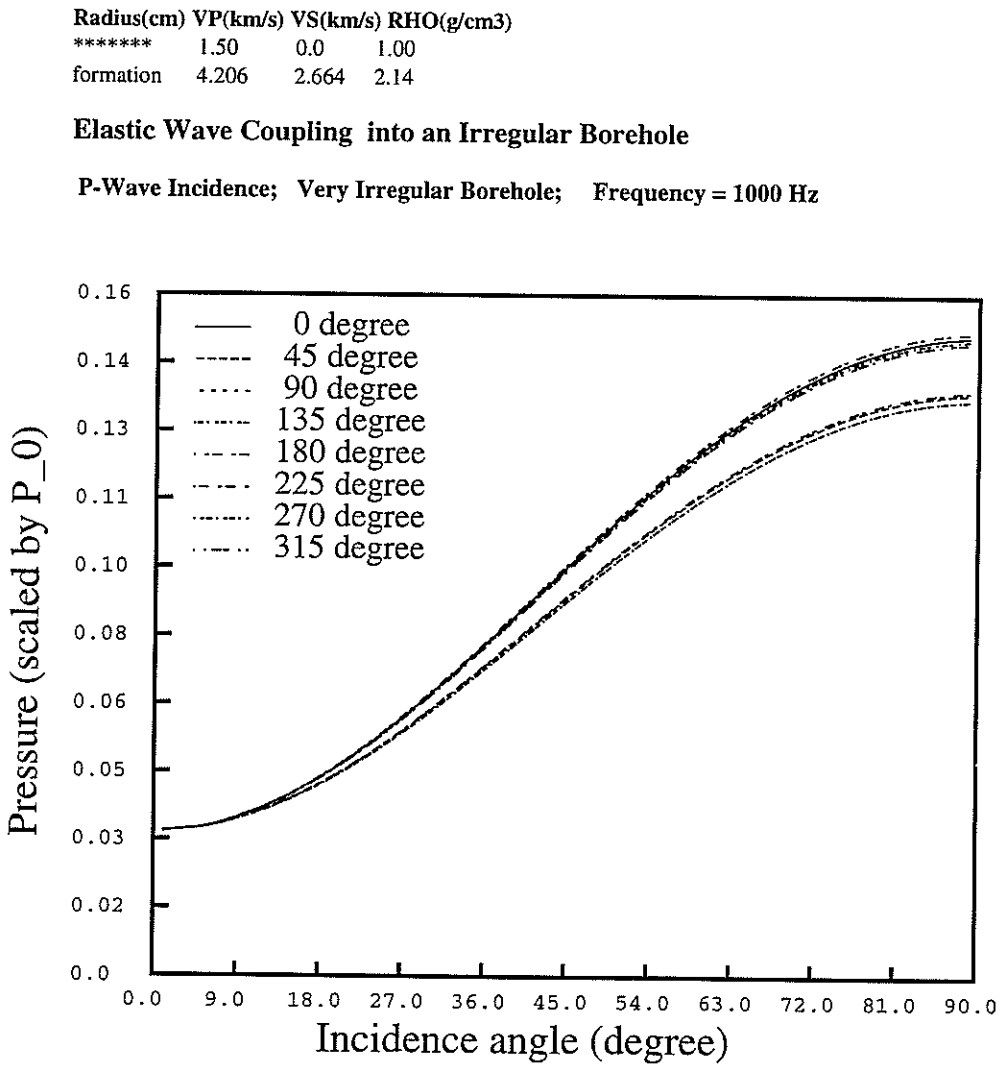

Figure 9: Pressure at the center of the fluid as a function of angle of incidence. The incident wave is a plane P-wave whose frequency is 1000 Hz. The formation is Berea sandstone. The borehole is shown in Figure 9. The pressure is scaled by the pressure of the incident P-wave. Shown in this figure are 8 curves with the azimuthal angle of the incident wave ranging from 0^o to 360^o in intervals of 45^o. The pressure in the irregular borehole splits into two distinct branches, depending on the azimuthal direction of the incident P-wave with respect to the effective major or minor axis of the borehole.

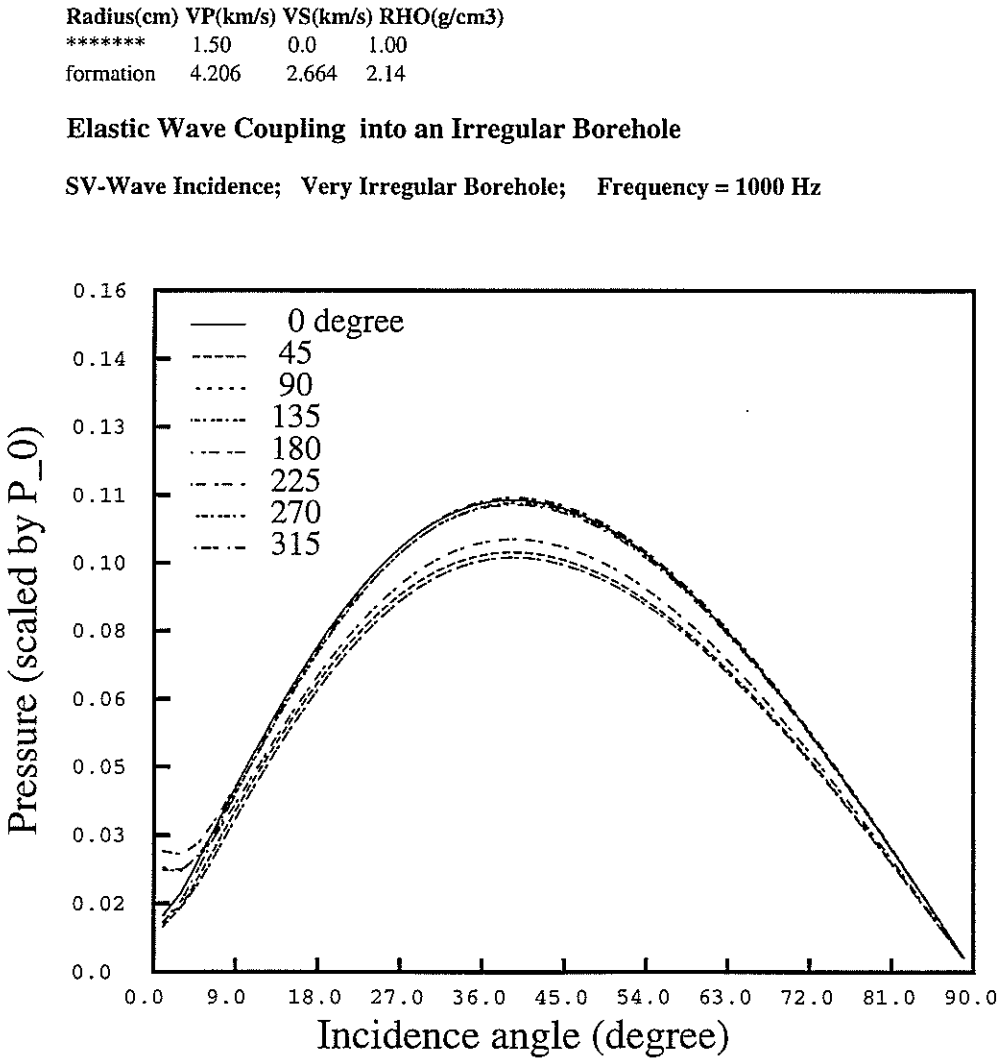

Figure 10: Pressure at the center of the fluid as a function of angle of incidence. The incident wave is a plane SV-wave whose frequency is 1000 Hz. The formation is Berea sandstone. The borehole is shown in Figure 9. A total of 8 curves are shown in this figure with the azimuthal angle of the incident wave ranging from 0^o to 360^o in intervals of 45^o. The pressure in the irregular borehole splits into two distinct branches, depending on the azimuthal direction of the incident SV-wave with respect to the effective major or minor axis of the borehole.

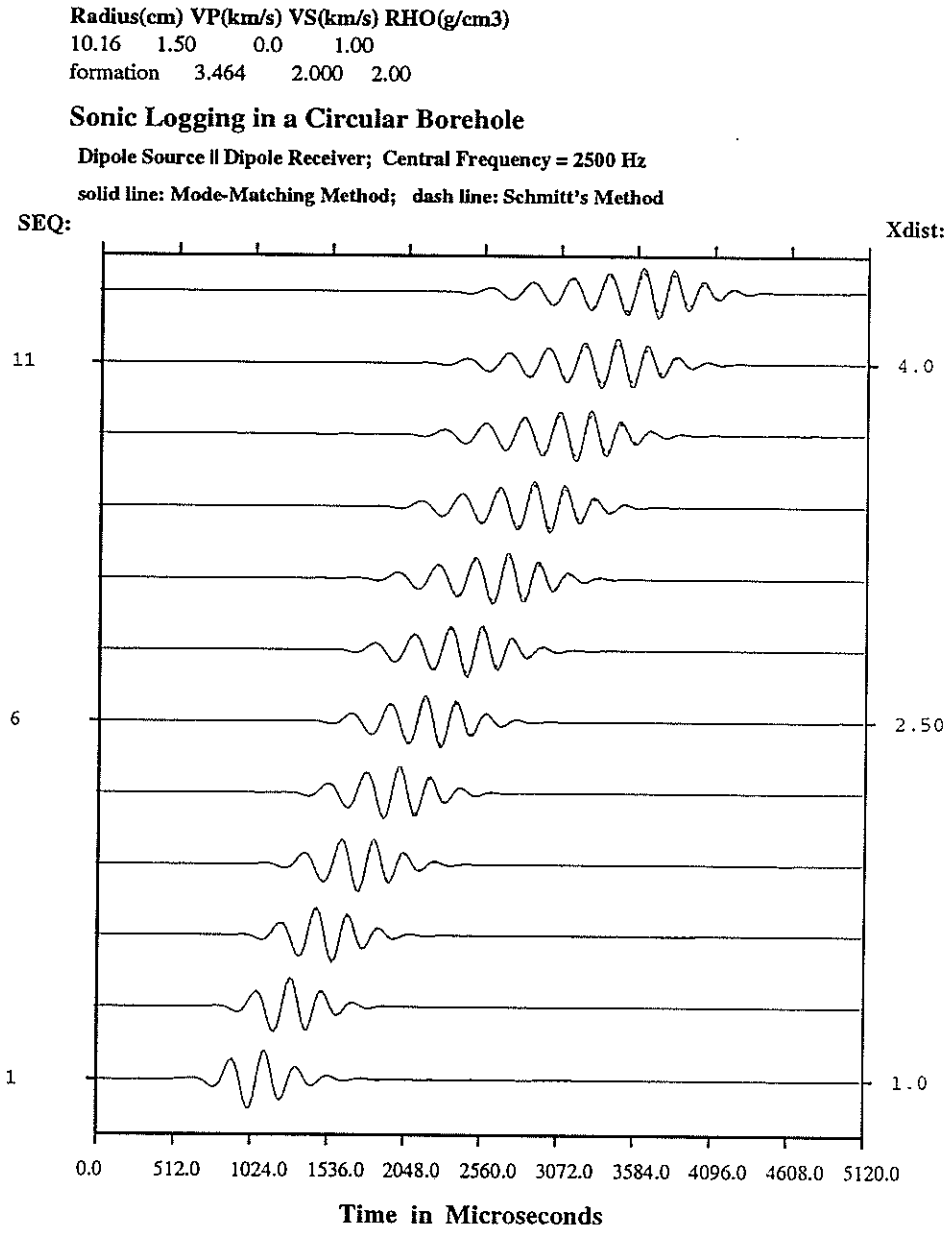

Figure 11: Comparison between the synthetic seismograms computed by the mode-matching method and by the classical discrete wavenumber method. The borehole is circular with a radius of 0.1016 m. The elastic parameters of the formation are: $\alpha = 3464\ m/s$, $\beta = 2000\ m/s$, and $\rho = 2.0\ g/cm^3$. A dipole source and an array of dipole receivers are used. Twelve (12) receivers are evenly distributed at offsets between 1.0 m and 4.3 m from the source. The source central frequency is 2500 Hz. The solid lines in this figure show the seismograms computed by the mode-matching method. The dashed lines are the ones computed by the discrete wavenumber method. The program for the discrete wavenumber method was written by D. P. Schmitt (1988).

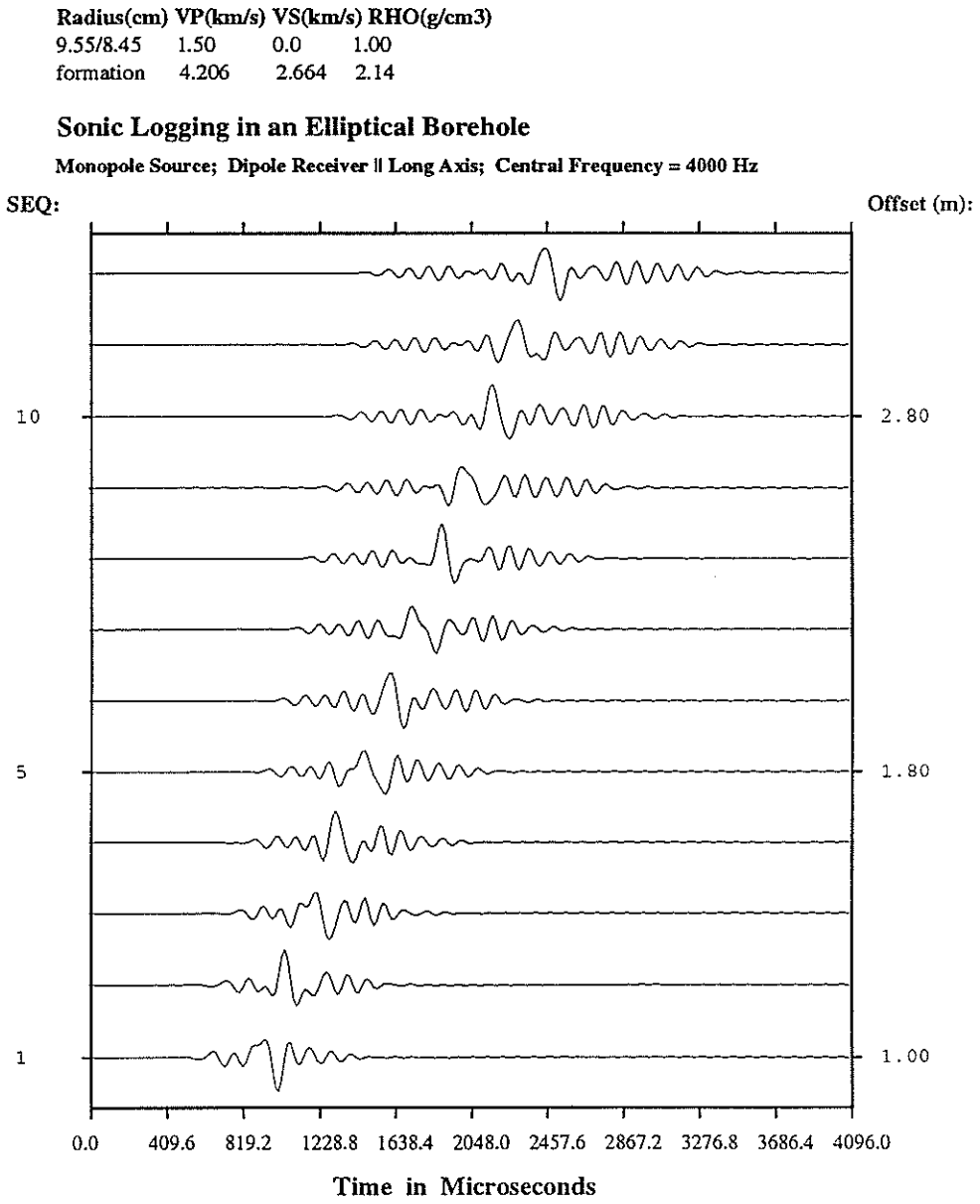

Figure 12: Synthetic seismograms in an elliptical borehole for a monopole source and an array of dipole receivers. The dipole receivers are polarized along the major axis of the borehole shown in Figure 2. The formation is Berea sandstone. The central frequency of the source is 4000 Hz. Twelve (12) receivers are evenly distributed at source-receiver offsets between 1.0 m and 3.2 m. The maximum amplitude is 0.833E+02.

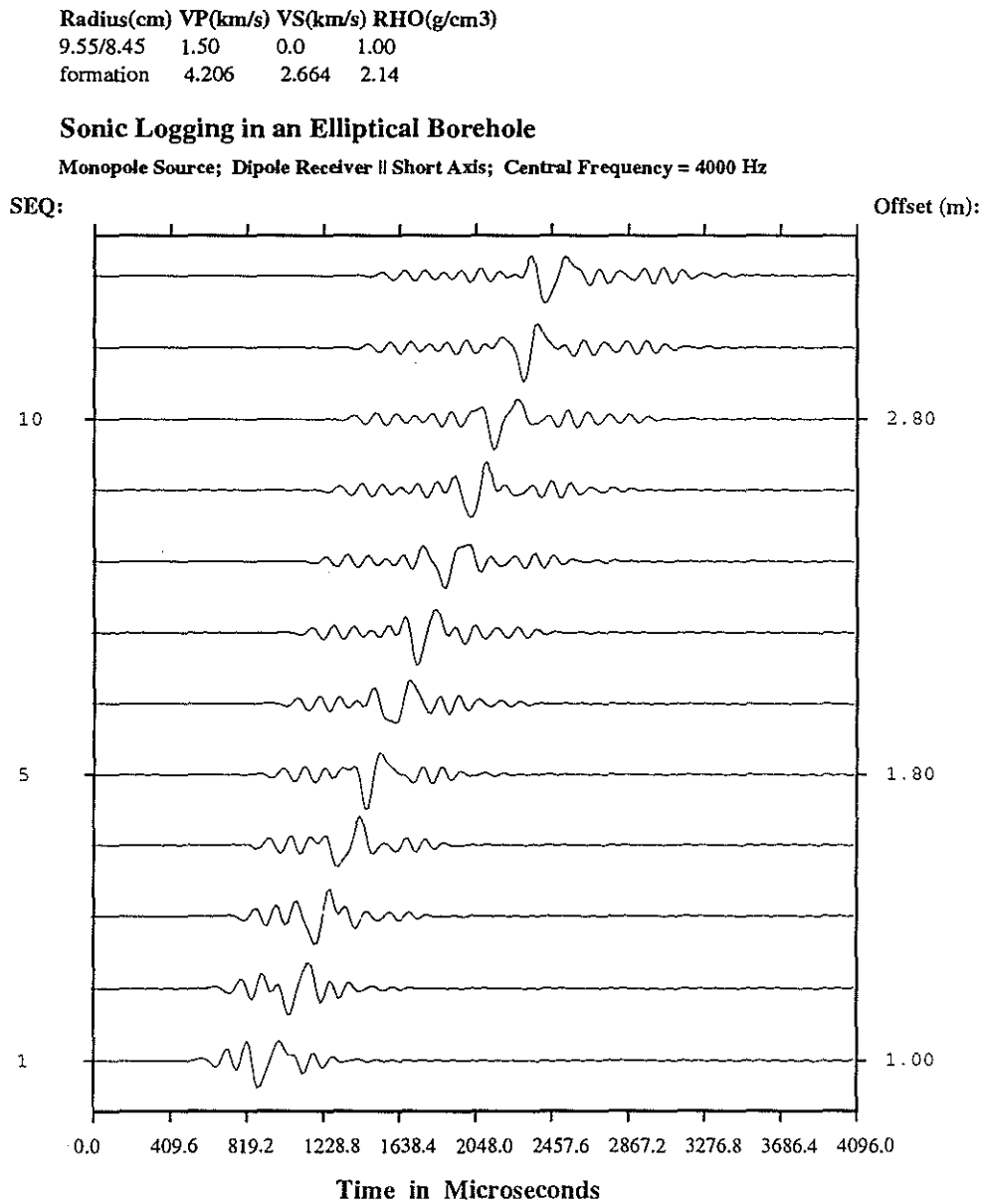

Figure 13: Synthetic seismograms in an elliptical borehole for a dipole source and an array of monopole receivers. The dipole source is polarized along the major axis of the borehole shown in Figure 2. The formation is Berea sandstone. The central frequency of the source is 4000 Hz. Twelve (12) receivers are evenly distributed at offsets between 1.0 m and 3.2 m from the source. The maximum amplitude is 0.136.

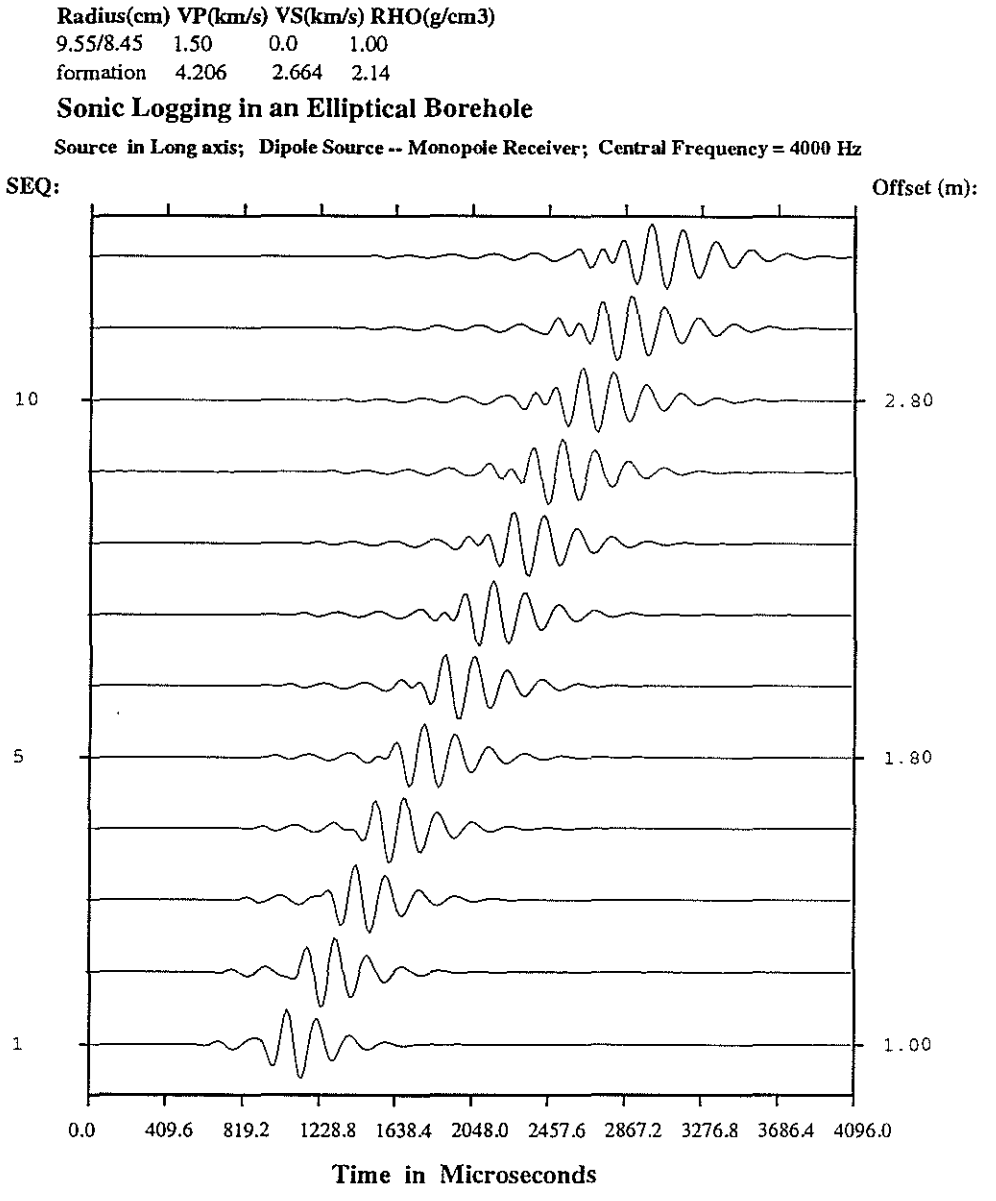

Figure 14: Synthetic seismograms in an elliptical borehole for a dipole source and an array of monopole receivers. The dipole source is polarized along the minor axis of the borehole shown in Figure 2. The formation is Berea sandstone. The central frequency of the source is 4000 Hz. Twelve (12) receivers are evenly distributed at offsets between 1.0 m and 3.2 m from the source. The maximum amplitude is 0.150.

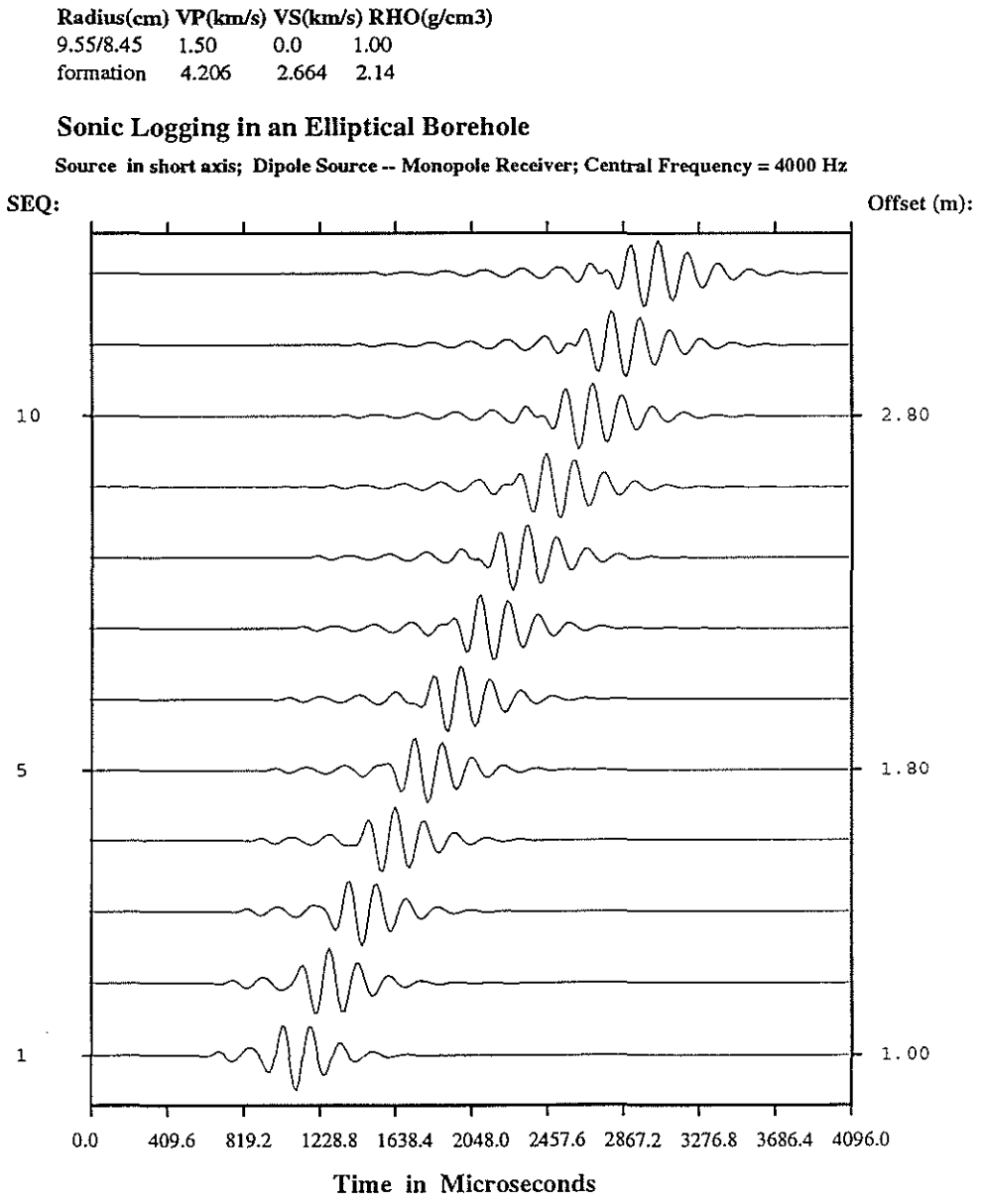

Figure 15: The Szegö polynomial $\psi_5(z)$ on the unit circle: (top) real part and (bottom) imaginary part. It is computed for the elliptical borehole shown in Figure 2.